A new class of central compact schemes with spectral-like resolution II: Hybrid weighted nonlinear schemes

Xuliang Liu[1], Shuhai Zhang[2], Hanxin Zhang[3] and Chi-Wang Shu[4]

Abstract

In this paper, we develop a class of nonlinear compact schemes based on our previous linear central compact schemes with spectral-like resolution [X. Liu, S. Zhang, H. Zhang and C-W. Shu, A new class of central compact schemes with spectral-like resolution I: Linear schemes, Journal of Computational Physics 248 (2013) 235-256]. In our approach, we compute the flux derivatives on the cell-nodes by the physical fluxes on the cell nodes and numerical fluxes on the cell centers. To acquire the numerical fluxes on the cell centers, we perform a weighted hybrid interpolation of an upwind interpolation and a central interpolation. Through systematic analysis and numerical tests, we show that our nonlinear compact scheme has high order, high resolution and low dissipation, and has the same ability to capture strong discontinuities as regular weighted essentially non-oscillatory (WENO) schemes. It is a good choice for the simulation of multiscale problems with shock waves.

Key Words: Compact scheme, WENO scheme, high resolution, low dissipation, weighted interpolation.

[1]State Key Laboratory of Aerodynamics, China Aerodynamics Research and Development Center, Mianyang, Sichuan 621000, China. E-mail: xlliu@foxmail.com. Research supported by the Chinese National Natural Science Foundation grant 11402291.

[2]State Key Laboratory of Aerodynamics, China Aerodynamics Research and Development Center, Mianyang, Sichuan 621000, China. E-mail: shuhai_zhang@163.com. Research supported by the Chinese National Natural Science Foundation grants 11172317, 11372340 and 91016001.

[3]China Aerodynamics Research and Development Center, Mianyang, Sichuan 621000, China. Research supported by the Chinese National Natural Science Foundation grant 91016001.

[4]Division of Applied Mathematics, Brown University, Providence, RI 02912, USA. E-mail: shu@dam.brown.edu. Research partially supported by NASA grant NNX12AJ62A and NSF grant DMS-1418750.

1 Introduction

There are two challenges in the design of high order numerical schemes for computational fluid dynamics, especially for high speed flows. The first is the possible presence of discontinuities or sharp transition layers. The second is the appearance of multiscale problems such as turbulence and aeroacoustics. The compressible turbulent flows are characterized by shocks or shocklets that result in a sudden change of fluid properties. All possible turbulent length scales and time scales must be resolved by the numerical method for the direct numerical simulation (DNS) of compressible turbulence. Thus, DNS requires numerical schemes that simultaneously have high-order accuracy and robust shock-capturing capability. The property of minimal dissipation and dispersion errors is likely to be significant for complex structures including smooth components such as vortices and acoustic waves, where the acoustic signals may be several orders of magnitude less energetic than the mean flow and could become confused with oscillations generated by stationary shock waves [2].

Traditional low order numerical methods, such as first order Godunov scheme [9] or Roe scheme [29], can resolve the discontinuities monotonically without spurious numerical oscillations. However, they often smear some of these discontinuities excessively. They also contain relatively large numerical dissipation in the smooth part of the solution. Hence many grid points are required to resolve complicated smooth structures such as vortices and acoustic waves, especially for long time simulation. The weighted essentially non-oscillatory (WENO) scheme is a popular high order numerical scheme for solving hyperbolic conservation laws. It is designed based on the essentially non-oscillatory (ENO) scheme in [11, 32, 33]. The WENO scheme was first proposed by Liu, Osher and Chan [19]. In this pioneering work, finite volume WENO schemes up to fourth order were designed. In 1996, Jiang and Shu [14] proposed a general framework to construct arbitrary order accurate finite difference WENO schemes, which are more efficient for multidimensional calculations. Both ENO and WENO use the idea of adaptive stencils in the reconstruction procedure based on the local smoothness of the numerical solution to automatically achieve high order accuracy and

non-oscillatory property near discontinuities. ENO uses just one (the smoothest one in some sense) of several candidate stencils in the reconstruction, while WENO uses a convex combination of all the candidate stencils, each being assigned a nonlinear weight which depends on the local smoothness of the numerical solution based on that stencil. WENO improves upon ENO in more efficiency, better smoothness of fluxes, and better steady state convergence. For more details of ENO and WENO schemes, we refer to the lecture notes and review paper by Shu [34, 35]. WENO schemes have two desirable properties that they capture discontinuities and maintain high order accuracy. It has been applied to many problems containing discontinuous solutions.

Even though the accuracy order of WENO schemes can be designed to be arbitrarily high, such as up to the eleventh order WENO schemes developed by Balsara and Shu [3], the resolution to short waves is not ideal, due to the numerical dispersion errors in these schemes. To overcome this drawback, there are efforts in the literature to modify the linear combination coefficients of a finite difference scheme to improve its dispersion properties, at the expense of lowering the order of accuracy. Based on this strategy, Tam and Webb [38] developed a dispersion relation preserving (DRP) finite difference scheme. Wang and Chen [40], Ponziani et al. [27] and Martin et al. [22] developed optimal WENO schemes.

The second drawback of these WENO schemes is that the numerical dissipation is relatively high, due to the upwind-biased stencil as well as the extra numerical dissipation provided through the nonlinear weights. The WENO methods provide sharp shock capturing, but overwhelms the physical dissipation and underpredicts approximately the upper three quarters of the resolvable wavenumbers for broadband problems [16]. Generally speaking, there are two methods to decrease the excessive dissipation of WENO schemes. One strategy is to use a hybrid scheme, i.e., in conjunction with low-dissipative algorithms for smooth parts of the flow. A key role for the success of hybrid methods is played by shock sensors that should be able to localize the necessary amount of numerical dissipation around shock waves. Adams and Shariff [1] first considered a truly adaptive hybrid discretization,

consisting of a compact upwind scheme coupled with a fifth-order ENO scheme. The method was expanded by Pirozzoli [24], who developed a fully conservative formulation by hybridizing a fifth-order compact upwind numerical flux with a seventh-order WENO flux, the switch being based on the local density gradient. Further improvements to hybrid WENO schemes were introduced by Ren et al. [28], in which the weight function is designed so that the abrupt transition from one sub-scheme to another is avoided and the resulting hybrid scheme is essentially oscillation free near the flow discontinuities. Another strategy is to use the central symmetrical stencils, other than upwind stencils, by including the contribution of the most downwind stencil. In the WENO-SYMBO schemes [22], the central symmetrical WENO scheme is used for better bandwidth efficiency with the optimal linear weights, however, the order of the WENO-SYMBO schemes in smooth regions of the solution may degenerate near certain critical points. Henrick et al. [12] devised a mapping function and applied it to the smoothness indicator of the original WENO scheme [14]. Compared to the original WENO scheme, the improved fifth-order WENO scheme (WENO-M) can achieve the optimal convergence order at critical points of smooth parts, reduce the numerical dissipation, and obtain sharper results near discontinuities. In [4], Borges et al. introduced another version of the fifth-order WENO scheme (WENO-Z) with a new smoothness indicator which is constructed by incorporating a global higher order smoothness measurement into the weights of the WENO scheme [14]. This method allows us to obtain the optimal convergence order at the critical points of smooth regions of the solution and captures shock in a physically sharp manner while maintaining stability and the essentially non-oscillatory behavior. Yamaleev and Carpenter [42, 43] proposed a family of energy stable WENO schemes, in which the central symmetrical stencils were used with the methodology of energy stable modifications. In [13], Hu et al. developed a sixth-order WENO-CU6 scheme, which used the nonlinear weighting relationship with a global smoothness indicator of the optimal higher order stencil.

The above approaches of modifying WENO schemes can achieve less numerical dissipation than the classical WENO schemes. However, these modified WENO schemes are still

considerably more dissipative than their linear counterparts. To simulate multiscale turbulence and acoustic waves, a good choice is the linear compact scheme, which has better dispersion behavior than an explicit finite difference scheme at the same order of accuracy. The most influential compact schemes for derivatives, interpolation and filtering were proposed by Lele [18]. Through systematic Fourier analysis, it is shown that these compact schemes have spectral-like resolution for short waves. The wave resolution of cell-centered compact schemes proposed by Lele [18] is much better than the resolution of cell-noded compact schemes. Through coupling the second derivatives, Mahesh [21] developed a family of compact schemes with good spectral-like resolution. Shukla and Zhong [36] developed a compact scheme for non-uniform meshes. Upwind compact schemes were also developed [7] for solving nonlinear hyperbolic problems. Nagarajan et al. [23] and Boersma [5] developed staggered compact schemes. However, the staggered compact schemes contain the cell-centered values, which should be obtained through interpolation from the values on cell nodes. Lele [18] proposed a compact interpolation to compute the values on the half-grid. In [20], Liu et al. developed a class of linear compact schemes based on the cell centered compact scheme of Lele [18]. These schemes equate a weighted sum of the nodal derivatives to a weighted sum of the function on both the cell-nodes and the cell-centers. This approach increases the memory requirement, however it does not increase the computational cost in the one-dimensional operator. Both the accuracy order and the wave resolution property are improved significantly.

Linear compact schemes have been widely used in the literature, especially for wave propagation problems in which nonlinearities are weak. However, it is known that application of standard central discretizations to high-Reynolds number fluid turbulence typically leads to numerical instability, owing to the accumulation of the aliasing errors resulting from discrete evaluation of the nonlinear convective terms. Linear compact schemes usually have no or low numerical dissipation. This is an advantage for the simulation of turbulence and acoustic waves, but it also causes problems for nonlinear hyperbolic problems with shock

waves or sharp gradients in the solution.

Filtering the computed solution is a commonly used practice to cure nonlinear instabilities of central schemes, while retaining high-order accuracy. High-order filters were introduced by Lele [18] and used by Visbal and Gaitonde [39] for the solution of conservation laws on stretched, curvilinear, and deforming meshes. Introducing WENO ideas to central schemes is another commonly used practice to cure nonlinear instabilities.

Based on the linear cell-centered compact scheme of Lele [18] and WENO schemes of Jiang and Shu [14], Deng et al. [8] and Jiang et al. [15] developed two types of WENO interpolation compact schemes. Zhang et al. [44] developed an increasingly higher order accuracy WENO interpolation method and formed a family of shock-capturing WENO compact schemes, for which the resolution of short waves is improved and numerical dissipation is reduced.

In this paper, we develop a new class of nonlinear compact schemes based on our previously developed linear central compact schemes with spectral-like resolution [20]. To acquire the numerical fluxes at cell centers, we perform a hybrid weighted nonlinear interpolation, which adapts between the central and upwind schemes smoothly by a new weighting strategy based on weighted factors and smoothness indicators. The new nonlinear compact schemes have higher spectral resolution than standard WENO schemes because they use more compact stencil information, and they have lower dissipation errors owing to the hybrid weighted upwind and central interpolation. Through a systematic analysis, tests and comparison, we show that the new nonlinear compact schemes have the same ability to capture strong discontinuities as the classical WENO schemes, while the resolution for high frequency waves in the solution is improved.

This paper is organized as follows. In Section 2, we derive the formulae for the hybrid weighted nonlinear schemes. The time advancement method is shown in Section 3. The numerical accuracy tests are performed in Section 4. In Section 5, we systemically analyze the dispersion and dissipation characteristics of the schemes. Numerical experiments including strong shock waves are shown in Section 6. Section 7 contains concluding remarks.

2 Scheme formulation

In this section, we present the methodology to develop our nonlinear compact schemes. We consider numerical approximations to the solution of the conservation law

$$\frac{\partial u}{\partial t} + \frac{\partial f(u)}{\partial x} = 0 \tag{2.1}$$

A semidiscrete finite difference can be represented as

$$\left(\frac{\partial u}{\partial t}\right)_j = -f'_j \tag{2.2}$$

where f'_j is the approximation to the spatial derivative $\frac{\partial f(u)}{\partial x}$ at the grid node x_j. We start our work from the linear central compact schemes [20]. Then we extend these linear schemes to nonlinear schemes.

2.1 Linear central compact schemes

In [20], we proposed a class of central compact schemes with spectral-like resolution (CCSSR), which are linear schemes termed CCSSR-L and has the following form

$$\begin{aligned} &\beta f'_{j-2} + \alpha f'_{j-1} + f'_j + \alpha f'_{j+1} + \beta f'_{j+2} \\ &\quad = a\frac{f_{j+\frac{1}{2}} - f_{j-\frac{1}{2}}}{\Delta x} + b\frac{f_{j+1} - f_{j-1}}{2\Delta x} + c\frac{f_{j+\frac{3}{2}} - f_{j-\frac{3}{2}}}{3\Delta x} \\ &\quad + d\frac{f_{j+2} - f_{j-2}}{4\Delta x} + e\frac{f_{j+\frac{5}{2}} - f_{j-\frac{5}{2}}}{5\Delta x} \end{aligned} \tag{2.3}$$

In this paper, we denote the central compact schemes with spectral-like resolution as "CCSSR" rather than "CCS" in our previous paper [20]. The relationships among the coefficients α, β, a, b, c, d and e are derived by matching the Taylor series coefficients of various orders. The detailed relationships of these coefficients are listed in [20]. The accuracy order of these schemes ranges from second to fourteenth. The stencil of the CCSSR-L schemes is shown in Figure 2.1.

In this paper, we focus on two tridiagonal schemes.

1. The fourth order linear scheme:

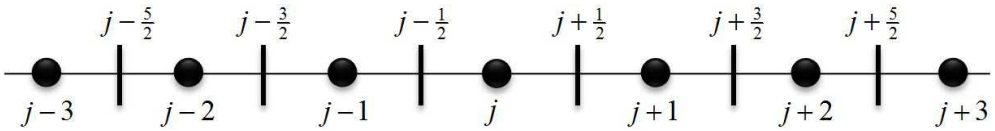

Figure 2.1: The stencil of the CCSSR schemes

The fourth order CCSSR-L4 has the following form

$$\alpha f'_{j-1} + f'_j + \alpha f'_{j+1} = a\frac{f_{j+\frac{1}{2}} - f_{j-\frac{1}{2}}}{\Delta x} + b\frac{f_{j+1} - f_{j-1}}{2\Delta x} \tag{2.4}$$

At the inner points, we choose $\alpha = \frac{1}{22}$, $a = \frac{12}{11}$, $b = 0$. At the boundary points, we choose $\alpha = 0$, $a = \frac{4}{3}$, $b = -\frac{1}{3}$.

2. The sixth order linear scheme:

The sixth order CCSSR-L6 has the following form

$$\alpha f'_{j-1} + f'_j + \alpha f'_{j+1} = a\frac{f_{j+\frac{1}{2}} - f_{j-\frac{1}{2}}}{\Delta x} + b\frac{f_{j+1} - f_{j-1}}{2\Delta x} + c\frac{f_{j+\frac{3}{2}} - f_{j-\frac{3}{2}}}{3\Delta x} \tag{2.5}$$

At the inner points, we choose $\alpha = -\frac{1}{12}$, $a = \frac{16}{9}$, $b = -\frac{17}{18}$, $c = 0$. At the boundary points, we choose $\alpha = 0$, $a = \frac{3}{2}$, $b = -\frac{3}{5}$, $c = \frac{1}{10}$.

The derivatives f'_j can be obtained by solving the linear systems of (2.3), (2.4) or (2.5). Equation (2.3) is a pentadiagonal system and equations (2.4) and (2.5) are tridiagonal systems. Hence, the fourth-order scheme (2.4) and sixth-order scheme (2.5) are more efficient and economical comparing with the pentadiagonal scheme (2.3), because they require only a tridiagonal matrix solver such as the Thomas algorithm that is easy and fast for actual computation. Both the fourth order and the sixth order schemes contain the values on the cell-centers $f_{j+\frac{1}{2}}$, which are unknown. There are many methods to compute the values on the cell-centers. High order linear compact interpolation [18] and WENO interpolation [44] are two typical examples. In our linear scheme [20], we used the same scheme as that for the node to compute the derivatives at cell centers and the physical values on cell centers by marching the physical equation. In this paper, we propose a new hybrid nonlinear interpolation to achieve the goal of computing flows with discontinuities and shock waves in a stable fashion.

2.2 Hybrid weighted nonlinear interpolation

2.2.1 Basic idea of the weighted interpolation

In [44], Zhang et al. proposed a method to weighted interpolate the physical values on cell interfaces. Here, we give a brief review for the process of the WENO interpolation.

The value on a cell center can be interpolated locally from the values on a stencil. In general, we can get a $(2r-1)$-th order approximation based on the flux function in a stencil $S^{2r-1} = (x_{i-r+1}, ..., x_{i+r-1})$. Using this stencil, the flux at any point can be evaluated as an interpolating polynomial:

$$\hat{f}^{2r-1}(x) = f_i + \sum_{l=1}^{2(r-1)} a_l (x - x_i)^l \tag{2.6}$$

Evaluating the function at the cell center $x_{i+\frac{1}{2}}$, the $(2r-1)$-th order approximation is given by

$$\hat{f}^L_{i+\frac{1}{2}} = q^{2r-1}(f_{i-r+1}, ..., f_{i+r-1}) \tag{2.7}$$

For the WENO interpolation in [30, 6], based on the WENO reconstruction idea in [14], the stencil S^{2r-1} can be divided into r sub-stencils

$$S^{2r-1}_k = (x_{i+k-r+1}, x_{i+k-r+2}, ..., x_{i+k}), \qquad k = 0, 1, ..., r-1$$

In each of these substencils, the r-th order approximation can be obtained

$$\hat{f}^{(k)}_{i+\frac{1}{2}} = q^r_k(f_{i+k-r+1}, ..., f_{i+k}) \tag{2.8}$$

where

$$q^r_k(g_0, ..., g_{r-1}) = \sum_{l=0}^{r-1} a^r_{k,l} g_l$$

Here, $a^r_{k,l},\ 0 \le k, l \le r-1$, are constant coefficients.

The value $\hat{f}^L_{i+\frac{1}{2}}$ can also be obtained by a linear combination of $\hat{f}^{(k)}_{i+\frac{1}{2}}$

$$q^{2r-1}(f_{i-r+1}, ..., f_{i+r-1}) = \sum_{k=0}^{r-1} d^r_k q^r_k(f_{i+k-r+1}, ..., f_{i+k}) \tag{2.9}$$

The approximation (2.9) is linear. The resulting scheme can not capture shock waves and other discontinuities without oscillations. Adopting the WENO idea, we use nonlinear weights ω_k^r to replace the linear weights d_k^r and obtain a nonlinear approximation

$$\hat{f}_{i+\frac{1}{2}} = \sum_{k=0}^{r-1} \omega_k^r q_k^r(f_{i+k-r+1}, ..., f_{i+k}) \tag{2.10}$$

where the nonlinear weight ω_k^r for the stencil S_k^{2r-1} is given by:

$$\omega_k^r = \frac{\alpha_k^r}{\alpha_0^r + \alpha_1^r + ... + \alpha_{r-1}^r} \tag{2.11}$$

with

$$\alpha_k^r = \frac{d_k^r}{(\epsilon + IS_k^r)^p}, \qquad k = 0, 1, ..., r-1$$

Here ϵ is a small positive number which is introduced to avoid the denominator becoming zero. IS_k is the smoothness indicator of the flux function in the k-th substencil which adopts the formulae given by Jiang and Shu [14] as

$$IS_k^r = \sum_{l=1}^{r-1} \int_{x_{i-\frac{1}{2}}}^{x_{i+\frac{1}{2}}} \triangle x^{2l-1} \left(\frac{\partial^l f^{(r)}(x)}{\partial^l x} \right)^2 dx. \tag{2.12}$$

2.2.2 Fourth order hybrid weighted nonlinear interpolation

The three second order interpolations in the substencils are

$$\begin{array}{l} \hat{f}_{j+\frac{1}{2}}^{(0)} = \frac{1}{2}(-f_{j-1} + 3f_j) \\ \hat{f}_{j+\frac{1}{2}}^{(1)} = \frac{1}{2}(f_j + f_{j+1}) \\ \hat{f}_{j+\frac{1}{2}}^{(2)} = \frac{1}{2}(3f_{j+1} - f_{j+2}) \end{array} \tag{2.13}$$

The linear third order upwind interpolation in the upwind stencil is given by

$$\hat{f}_{j+\frac{1}{2}}^{\text{upwind}} = \frac{1}{8}(-f_{j-1} + 6f_j + 3f_{j+1}) \tag{2.14}$$

The linear fourth order central interpolation in the central stencil is given by

$$\hat{f}_{j+\frac{1}{2}}^{\text{central}} = \frac{1}{16}(-f_{j-1} + 9f_j + 9f_{j+1} - f_{j+2}) \tag{2.15}$$

The upwind interpolation has better stability, while the central interpolation has lower dissipation. In this paper, we use the hybrid method of Ren et al. [28] to balance the stability and dissipation of the scheme. Let the hybrid weighted linear interpolation in the central global stencil be

$$\hat{f}_{j+\frac{1}{2}}^{\text{hybrid}} = (1-\sigma)\,\hat{f}_{j+\frac{1}{2}}^{\text{upwind}} + \sigma \hat{f}_{j+\frac{1}{2}}^{\text{central}} = \sum_{r=0}^{2} d_r \hat{f}_{j+\frac{1}{2}}^{(r)} \tag{2.16}$$

That is

$$\hat{f}_{j+\frac{1}{2}}^{\text{hybrid}} = -\frac{d_0}{2} f_{j-1} + \frac{3d_0+d_1}{2} f_j + \frac{d_1+3d_2}{2} f_{j+1} - \frac{d_2}{2} f_{j+2} \tag{2.17}$$

The linear weights are

$$d_0 = \frac{2-\sigma}{8}, \;\; d_1 = \frac{6}{8}, \;\; d_2 = \frac{\sigma}{8} \tag{2.18}$$

The weight $0 \le \sigma \le 1$, which controls the contribution of the upwind or central interpolation. If $\sigma = 1$, the interpolation is completely central. It is completely upwind when $\sigma = 0$. Ren et al. [28] gave a definition of σ as follows

$$\sigma = \min\left(1, \; \frac{r_{j+\frac{1}{2}}}{r_c}\right) \tag{2.19}$$

where $r_{j+\frac{1}{2}} = \min(r_j, r_{j+1})$, and r_j is defined by

$$r_j = \frac{|2\,(f_{j+1}-f_j)\,(f_j - f_{j-1})| + \delta}{(f_{j+1}-f_j)^2 + (f_j - f_{j-1})^2 + \delta} \tag{2.20}$$

where the positive parameter δ is given by

$$\delta = \frac{0.9 r_c}{1 - 0.9 r_c} \times 10^{-6} \tag{2.21}$$

The constant r_c is a threshold. The larger its value, the more dissipation the numerical scheme becomes. In this paper, we set $r_c = 0.5$ for all the numerical examples.

The smoothness indicators are

$$\begin{aligned}
IS_0 =& f_{j-1}\,(f_{j-1} - 2f_j) + f_j^2 \\
IS_1 =& f_j\,(f_j - 2f_{j+1}) + f_{j+1}^2 \\
IS_2 =& \frac{1}{2880}[f_{j-1}\,(6649 f_{j-1} - 30414 f_j + 23094 f_{j+1} - 5978 f_{j+2}) \\
&+ 3 f_j\,(13667 f_j - 23534 f_{j+1} + 6338 f_{j+2}) \\
&+ 3 f_{j+1}\,(11147 f_{j+1} - 6458 f_{j+2}) + 3169 f_{j+2}^2]
\end{aligned} \tag{2.22}$$

With these smoothness indicators, we can compute the nonlinear weights by [4, 13]

$$\omega_r = \frac{\alpha_r}{\sum_{s=0}^{2} \alpha_s}, \quad \alpha_r = d_r \left(\mathrm{C} + \frac{\tau_4}{\epsilon + IS_r} \right), \quad r = 0, ..., 2 \tag{2.23}$$

where ϵ is a small positive number used to avoid the denominator becoming zero. We take it as $\epsilon = 10^{-40}$. Eq. (2.23) has a similar form as the WENO-CU6 scheme of Hu et al. [13]. A parameter C is introduced to increase the contribution of the optimal linear weights. It can be found that, increasing or decreasing the value of C only changes the numerical dissipation slightly. The larger the value of C is, the less numerical dissipation the numerical scheme has. However, since excessively large values of C may lead to numerical instabilities for problems with strong shock waves [13], we set $C = 5$ for all the numerical examples.

The reference smoothness indicator is defined by

$$\tau_4 = IS_2 - \frac{1}{2}\left(IS_0 + IS_1\right) \tag{2.24}$$

For the regular WENO scheme [14], Henrich et al. [12] pointed out that the nonlinear weights with the smoothness indicator in [14] may lose accuracy at certain smooth extrema. To solve this problem, they introduced a mapping function

$$g_r(\omega) = \frac{\omega(d_r + d_r^2 - 3d_r\omega + \omega^2)}{d_r^2 + \omega(1 - 2d_r)} \tag{2.25}$$

which recovers the approximating accuracy order of ω_r to the linear weights d_r at critical points. $g_r(\omega)$ is a non-decreasing monotone function with the following properties:

1. $0 \le g_r(\omega) \le 1$, $g_r(0) = 0$ and $g_r(1) = 1$.
2. $g_r(\omega) \approx 0$ if $\omega \approx 0$; $g_r(\omega) \approx 1$ if $\omega \approx 1$.
3. $g_r(d_r) = d_r$, $g_r'(d_r) = g_r''(d_r) = 0$.

In this paper, we also use the mapping function for the nonlinear interpolation. The modified nonlinear weights are

$$\omega_r^M = \frac{\alpha_r^M}{\sum_{s=0}^{2} \alpha_s^M}, \qquad \alpha_r^M = g_r(\omega_r), \quad r = 0, \cdots, 2$$

Here a superscript (M) has been added to signify the weights using the mapping function. Numerical results in [12] confirmed the usefulness of the mapping, since with the modified weights the resulting WENO-M scheme recovered the formal order of convergence at critical points of a smooth solution.

The final fourth order hybrid weighted nonlinear mapping interpolation is defined by

$$\hat{f}_{j+\frac{1}{2}} = \sum_{r=0}^{2} \omega_r^M \hat{f}_{j+\frac{1}{2}}^{(r)} = -\frac{\omega_0^M}{2} f_{j-1} + \frac{3\omega_0^M + \omega_1^M}{2} f_j + \frac{\omega_1^M + 3\omega_2^M}{2} f_{j+1} - \frac{\omega_2^M}{2} f_{j+2} \tag{2.26}$$

Substituting this fourth order hybrid weighted interpolation into the fourth order linear scheme (2.4), we can obtain a fourth order nonlinear compact scheme. We mark it as CCSSR-HW4.

2.2.3 Sixth order hybrid weighted nonlinear interpolation

The four third order interpolations in the substencils are

$$\begin{aligned} \hat{f}_{j+\frac{1}{2}}^{(0)} &= \tfrac{1}{8}(3f_{j-2} - 10f_{j-1} + 15f_j) \\ \hat{f}_{j+\frac{1}{2}}^{(1)} &= \tfrac{1}{8}(-f_{j-1} + 6f_j + 3f_{j+1}) \\ \hat{f}_{j+\frac{1}{2}}^{(2)} &= \tfrac{1}{8}(3f_j + 6f_{j+1} - f_{j+2}) \\ \hat{f}_{j+\frac{1}{2}}^{(3)} &= \tfrac{1}{8}(15f_{j+1} - 10f_{j+2} + 3f_{j+3}) \end{aligned} \tag{2.27}$$

The fifth order upwind interpolation in the upwind stencil is given by

$$\hat{f}_{j+\frac{1}{2}}^{\text{upwind}} = \frac{1}{128}\left(3f_{j-2} - 20f_{j-1} + 90f_j + 60f_{j+1} - 5f_{j+2}\right) \tag{2.28}$$

The sixth order central interpolation in the central stencil is given by

$$\hat{f}_{j+\frac{1}{2}}^{\text{central}} = \frac{1}{256}\left(3f_{j-2} - 25f_{j-1} + 150f_j + 150f_{j+1} - 25f_{j+2} + 3f_{j+3}\right) \tag{2.29}$$

We let the hybrid weighted linear interpolation in the central stencil be

$$\hat{f}_{j+\frac{1}{2}}^{\text{hybrid}} = (1-\sigma)\,\hat{f}_{j+\frac{1}{2}}^{\text{upwind}} + \sigma \hat{f}_{j+\frac{1}{2}}^{\text{central}} = \sum_{r=0}^{3} d_r \hat{f}_{j+\frac{1}{2}}^{(r)} \tag{2.30}$$

That is

$$\begin{aligned} \hat{f}_{j+\frac{1}{2}}^{\text{hybrid}} =& \frac{3d_0}{8} f_{j-2} - \frac{10d_0 + d_1}{8} f_{j-1} + \frac{15d_0 + 6d_1 + 3d_2}{8} f_j \\ &+ \frac{3d_1 + 6d_2 + 15d_3}{8} f_{j+1} - \frac{d_2 + 10d_3}{8} f_{j+2} + \frac{3d_3}{8} f_{j+3} \end{aligned} \tag{2.31}$$

The linear weights are

$$d_0 = \frac{2-\sigma}{32}, \quad d_1 = \frac{5\,(4-\sigma)}{32}, \quad d_2 = \frac{5\,(2+\sigma)}{32}, \quad d_3 = \frac{\sigma}{32} \tag{2.32}$$

The weight σ controls the upwind or central interpolation, which is a continuous function as Eq.(2.19), where $r_{j+\frac{1}{2}} = \min\left(r_{j-1}, r_j, r_{j+1}, r_{j+2}\right)$. The larger the threshold value of r_c is, the more numerical dissipation the numerical scheme has. Like that in fourth order scheme, we again set $r_c = 0.5$ for all numerical examples in this paper. r_j is defined as Eq.(2.20). The positive parameter δ is given as Eq.(2.21).

The smoothness indicators are

$$\begin{aligned}
IS_0 &= \tfrac{1}{3}[f_{j-2}\left(4f_{j-2} - 19f_{j-1} + 11f_j\right) + f_{j-1}\left(25f_{j-1} - 31f_j\right) + 10f_j^2] \\
IS_1 &= \tfrac{1}{3}[f_{j-1}\left(4f_{j-1} - 13f_j + 5f_{j+1}\right) + 13f_j\left(f_j - f_{j+1}\right) + 4f_{j+1}^2] \\
IS_2 &= \tfrac{1}{3}[f_j\left(10f_j - 31f_{j+1} + 11f_{j+2}\right) + f_{j+1}\left(25f_{j+1} - 19f_{j+2}\right) + 4f_{j+2}^2] \\
IS_3 =& \frac{1}{232243200}[f_{j-2}(525910327f_{j-2} - 4562164630f_{j-1} + 7799501420f_j \\
&- 6610694540f_{j+1} + 2794296070f_{j+2} - 472758974f_{j+3}) + 5f_{j-1}(2146987907f_{j-1} \\
&- 7722406988f_j + 6763559276f_{j+1} - 2926461814f_{j+2} + 503766638f_{j+3}) \\
&+ 20f_j\left(1833221603f_j - 3358664662f_{j+1} + 1495974539f_{j+2} - 263126407f_{j+3}\right) \\
&+ 20f_{j+1}\left(1607794163f_{j+1} - 1486026707f_{j+2} + 268747951f_{j+3}\right) \\
&+ 5f_{j+2}\left(1432381427f_{j+2} - 536951582f_{j+3}\right) + 263126407f_{j+3}^2]
\end{aligned} \tag{2.33}$$

The nonlinear weights are

$$\omega_r = \frac{\alpha_r}{\sum_{s=0}^{3}\alpha_s}, \quad \alpha_r = d_r\left(\mathrm{C} + \frac{\tau_6}{\epsilon + IS_r}\right), \quad r = 0, ..., 3 \tag{2.34}$$

Here, we take $\epsilon = 10^{-40}$. Following the fourth order interpolation, we set $C = 5$ for all numerical examples.

The reference smoothness indicator is defined by

$$\tau_6 = IS_3 - \frac{1}{8}\left(IS_0 + 6IS_1 + IS_2\right) \tag{2.35}$$

Using the mapping function as Eq.(2.25), the mapped nonlinear weights are

$$\omega_r^M = \frac{\alpha_r^M}{\sum_{s=0}^{3}\alpha_s^M}, \qquad \alpha_r^M = g_r(\omega_r), \quad r = 0, \cdots, 3 \tag{2.36}$$

The final sixth order hybrid weighted nonlinear mapping interpolation is

$$\begin{aligned}\hat{f}_{j+\frac{1}{2}} = \sum_{r=0}^{3} \omega_r^M \hat{f}_{j+\frac{1}{2}}^{(r)} =& \frac{3\omega_0^M}{8} f_{j-2} - \frac{10\omega_0^M + \omega_1^M}{8} f_{j-1} + \frac{15\omega_0^M + 6\omega_1^M + 3\omega_2^M}{8} f_j \\ &+ \frac{3\omega_1^M + 6\omega_2^M + 15\omega_3^M}{8} f_{j+1} - \frac{\omega_2^M + 10\omega_3^M}{8} f_{j+2} + \frac{3\omega_3^M}{8} f_{j+3}\end{aligned} \tag{2.37}$$

Substituting this sixth order hybrid weighted interpolation into the sixth order linear scheme (2.5), we can obtain a sixth order nonlinear compact scheme. We mark it as CCSSR-HW6.

2.2.4 Flux splitting

The purpose of flux splitting is to introduce correct upwinding. In general, the flux can be split into two parts:

$$f(u) = f^+(u) + f^-(u)$$

where

$$\frac{df^+(u)}{du} \geq 0 \ , \ \frac{df^-(u)}{du} \leq 0$$

We would need the positive and negative fluxes $f^{\pm}(u)$ to have as many derivatives as the order of the scheme. In this paper, we use the Lax-Friedrichs flux splitting

$$f^{\pm}(u) = \frac{1}{2}(f(u) \pm \alpha u) \tag{2.38}$$

where α is taken as $\alpha = \max_u \{|f'(u)|\}$ over the relevant range of u. For Euler equations, the α is chosen differently for each characteristic field as the maximum of the corresponding eigenvalue of the Jacobian in that field. We refer to [14] for the details.

During the weighted interpolation for the cell-centered value, we use the upwind biased stencil to get the value of mid-cell $f_{i+\frac{1}{2}}$. That is the value $f^+_{i+\frac{1}{2}}$ is interpolated from the point value in the stencil $S^+ = (x_{i-r+1}, ..., x_{i+r-1})$ and the value $f^-_{i+\frac{1}{2}}$ from $S^- = (x_{i-r+2}, ..., x_{i+r})$. We have only described how $\hat{f}^+_{i+\frac{1}{2}}$ is approximated because the formulas for the negative part of the split flux are symmetric to the positive part with respect to $x = x_{i+\frac{1}{2}}$. Also, for simplicity, we have dropped the '+' sign in the superscript.

3 Time advancement

After the spatial derivative is discretized, we obtain a system of initial value problems of ordinary differential equations (ODEs),

$$\frac{dU}{dt} = L(U) \tag{3.1}$$

where the operator $L(U)$ is an approximation to the spatial derivative in the partial differential equations (PDEs). This set of ODEs can be discretized by the optimal third order TVD Runge-Kutta method [32, 10], which is given as follows:

$$\begin{aligned} U^{(1)} &= U^n + \Delta t L(U^n) \\ U^{(2)} &= \frac{3}{4}U^n + \frac{1}{4}U^{(1)} + \frac{1}{4}\Delta t L(U^{(1)}) \\ U^{n+1} &= \frac{1}{3}U^n + \frac{2}{3}U^{(2)} + \frac{2}{3}\Delta t L(U^{(2)}) \end{aligned} \tag{3.2}$$

This optimal third order TVD Runge-Kutta method can apply to general initial value problems of PDEs in any spatial dimensions. Higher order versions of such time discretizations can of course also be used.

4 Numerical accuracy tests

In this section, we test the numerical accuracy of the CCSSR-HW6 schemes for both scalar equations and Euler equations.

4.1 Scalar equation

We solve the following linear scalar equation:

$$\begin{aligned} u_t + u_x = 0, \qquad -1 \le x \le 1 \\ u(x, t=0) = u_0(x) \end{aligned} \tag{4.1}$$

with periodic boundary condition and two different initial conditions: $u_0(x) = \sin(\pi x)$, $u_0(x) = \sin(\pi x - \sin(\pi x)/\pi)$.

Schemes	N	L_1 error	L_1 order	L_∞ error	L_∞ order
CCSSR-HW6	10	0.359E-02	–	0.554E-02	–
	20	0.543E-04	6.05	0.147E-03	5.23
	40	0.927E-06	5.87	0.354E-05	5.38
	80	0.160E-07	5.86	0.810E-07	5.45
	160	0.189E-09	6.40	0.898E-09	6.49

Table 4.1: L_1 and L_∞ errors and numerical orders of accuracy on $u_t + u_x = 0$ with $u_0(x) = \sin(\pi x)$. N is the total number of grid points in a uniform mesh. $t = 1$.

Schemes	N	L_1 error	L_1 order	L_∞ error	L_∞ order
CCSSR-HW6	10	0.342E-01	–	0.763E-01	–
	20	0.114E-02	4.90	0.323E-02	4.56
	40	0.297E-04	5.27	0.112E-03	4.85
	80	0.802E-06	5.21	0.475E-05	4.56
	160	0.149E-07	5.75	0.150E-06	4.99

Table 4.2: L_1 and L_∞ errors and numerical orders of accuracy on $u_t + u_x = 0$ with $u_0(x) = \sin(\pi x - \sin(\pi x)/\pi)$. N is the total number of grid points in a uniform mesh. $t = 2$.

The grid is progressively refined from 10 points to 160 points for the convergence analysis. The initial CFL is 0.5 for the 10-points grid and is reduced by a factor of $2^{\frac{(3-r)}{3}}$ for r-th order scheme at each refinement.

In Tables 4.1-4.2, the L_1 and L_∞ errors and numerical orders of accuracy are given for the CCSSR-HW6 scheme for the different initial conditions. We can observe that the designed orders of accuracy are achieved in all cases, at least in L_1 norm. If we use quadruple precision and continue further refining the mesh, we can see the designed sixth order of accuracy for both the L_1 and the L_∞ norms eventually. We do not present these results to save space.

Schemes	N	L_1 error	L_1 order	L_∞ error	L_∞ order
CCSSR-HW6	10	0.170E-03	–	0.259E-03	–
	20	0.386E-05	5.46	0.854E-05	4.92
	40	0.616E-07	5.97	0.183E-06	5.54
	80	0.495E-09	6.96	0.777E-09	7.88
	160	0.773E-11	6.00	0.121E-10	6.00

Table 4.3: L_1 and L_∞ errors and numerical orders of accuracy for one-dimensional Euler equation with CCSSR-HW6 scheme. N is the total number of grid points in a uniform mesh. $t = 1$.

4.2 Euler equations

The advection of a smooth density wave over a periodic domain is considered for the one dimensional Euler equations. The pressure and velocity are constants, thus reducing the Euler equations to a linear advection equation for the density, with the advection speed as the freestream velocity. The exact solution is given by:

$$(\rho, u, p) = (1 + 0.1 \sin [\pi (x - t)], 1, 1)$$

The computational domain is taken to be [0, 2]. We solve the equations up to $t = 1$ with periodic boundary condition. The grid is progressively refined from 10 points to 160 points for the convergence analysis. The initial CFL is 0.5 for the 10-points grid and is reduced by a factor of $2^{\frac{(3-r)}{3}}$ for r-th order scheme at each refinement.

In Table 4.3, the L_1 and L_∞ errors of density and numerical orders of accuracy are given for the CCSSR-HW6 schemes. We can observe that the designed order of accuracy is achieved.

For the two dimensional Euler equation, the test function is:

$$(\rho, u, v, p) = (1 + 0.2 \sin [\pi (x + y - 2t)], 1, 1, 1)$$

The computational domain is taken to be $[0,\ 2]\times[0,\ 2]$. We solve the equation up to $t = 0.5$ with periodic boundary condition. The grid is progressively refined from 10×10

Schemes	N × N	L_1 error	L_1 order	L_∞ error	L_∞ order
CCSSR-HW6	10×10	0.340E-03	–	0.518E-03	–
	20×20	0.782E-05	5.44	0.174E-04	4.90
	40×40	0.150E-06	5.70	0.480E-06	5.18
	80×80	0.119E-08	6.98	0.255E-08	7.55
	160×160	0.155E-10	6.27	0.243E-10	6.72

Table 4.4: L_1 and L_∞ errors and numerical orders of accuracy for two-dimensional Euler equation with CCSSR-HW6 scheme. N is the total number of grid points in a uniform mesh. $t = 0.5$.

points to 160×160 points for the convergence analysis. The initial CFL is 0.5 for the 10×10 points grid and is reduced by a factor of $2^{\frac{(3-r)}{3}}$ for r-th order scheme at each refinement.

In Table 4.4, the L_1 and L_∞ errors of density and numerical orders of accuracy are given for the CCSSR-HW6 schemes. We can observe that the designed order of accuracy is achieved.

5 The analysis of the dispersion and dissipation characteristics

In this section, we analyze the dispersion and dissipation characteristics of CCSSR-HW. It is well known that the order of the truncation error of a numerical scheme only provides information on the asymptotic convergence rate to the exact solution, but it does not convey any information on the actual error on a finite computational grid; rather, wave-propagation characteristics of a difference scheme provide information on all the Fourier components supported on the grid [25].

For the purpose of the analysis of the spectral properties, let us consider the one-dimensional propagation of small disturbances in a periodic domain $[0, 2\pi]$, governed by the linear advection equation, with monochromatic sinusoidal initial conditions of wavelength λ

and wavenumber $k = \frac{2\pi}{\lambda}$,

$$\frac{\partial f}{\partial t} + c\frac{\partial f}{\partial x} = 0, \quad x \in [0, 2\pi], \quad f(x, 0) = \hat{f}_0 e^{ikx} \tag{5.1}$$

where $i = \sqrt{-1}$ and $c > 0$. We consider a semi-discrete approximation of Eq. (5.1) on a grid with uniform spacing $h = \frac{2\pi}{N}$ and nodes $x_j = j \cdot h$, $j = 0, \cdots, N$,

$$\frac{df_j}{dt} + cf'_j = 0, \quad f_j(0) = \hat{f}_0 e^{ijw} \tag{5.2}$$

where $w = k \cdot h$ is the so-called reduced wavenumber [18]. If one assumes a linear compact finite-difference approximation for the spatial derivative of f

$$\sum_p b_p f'_{j+p} = \frac{1}{h} \sum_q a_q f_{j+q} \tag{5.3}$$

then we could change the Eq. (5.2) to the form

$$\frac{d}{dt}\left(\sum_p b_p f_{j+p}\right) + c\left(\sum_p b_p f'_{j+p}\right) = 0 \tag{5.4}$$

In response to the Eq. (5.3) and Eq. (5.4), we can obtain the exact solution [25] of the Eq. (5.2)

$$f_j(t) = \hat{f}_0 e^{ijw} e^{-i\frac{ct}{h}w'} \tag{5.5}$$

and w' is the "modified wavenumber" associated with the space discretization (5.3),

$$w'(w) = \frac{\sum_q a_q e^{iqw}}{i\sum_p b_p e^{ipw}} \tag{5.6}$$

where $w'(w) = w'_r(w) + iw'_i(w)$, $w'_r(w)$ is the real part of modified wavenumber, and $w'_i(w)$ is the imaginary part of modified wavenumber. In order to analyze the dispersion and dissipation characteristics, we substitute the real and imaginary part of modified wavenumber to Eq. (5.5),

$$f_j(t) = \hat{f}_0 e^{ijw} e^{-i\frac{ct}{h}w'} = \hat{f}_0 e^{ijw} e^{-i\frac{ct}{h}(w'_r + iw'_i)} = \hat{f}_0 e^{i(jw - \frac{ct}{h}w'_r)} e^{\frac{ct}{h}w'_i} \tag{5.7}$$

According to the Eq. (5.7), we can conclude that the real part of modified wavenumber is associated with the dispersion property of the discretization scheme, while the imaginary part of modified wavenumber is related to its dissipation property. Spectral schemes have $w'(w) = w$, in other words, $w'_r(w) = w$ and $w'_i(w) = 0$. Therefore the modified wavenumber $w'(w)$ can be usefully interpreted as a measure of the relative dispersion and dissipation error associated with the finite-difference discretization. The smaller the error $|w'_r(w) - w|$ is, the smaller the dispersion error is, in other words, the discretization schemes have better spectral resolution. The smaller the error $|w'_i(w) - 0|$ is, the smaller the dissipation error is.

The analysis of shock-capturing schemes is very difficult for their inherent nonlinearity, which prevents the straightforward application of the tools extensively used to evaluate linear schemes, for example Fourier analysis [18]. Nonlinearity also makes comparison of the relative quality of different methods, other than a case-by-case basis, almost impossible. Generally, classical shock-capturing schemes have linear counterparts that are used as guidance to improve their spectral behavior [44]. For example, freezing the nonlinear weights turns WENO schemes into linear upwind schemes, whose spectral transfer function has been used in the development of the optimized-WENO schemes [40, 27, 22]. However, numerical tests show that the nonlinear features have a dramatic impact on the performance of numerical schemes, and their actual behavior may be quite different from linear predictions [26].

For a nonlinear scheme, no analytical formula of the spectral relations can be obtained. However, the modified wavenumber of the nonlinear scheme in terms of the approximate dispersion relation (ADR) can be obtained using the technique of Pirozzoli [25].

The main results of the CCSSR-HW4, CCSSR-HW6 and WENO5 schemes using the ADR method [25] are reported in Figure 5.1, in terms of the real and the imaginary part of the modified wavenumber (w'). The spectral properties (both dispersion and dissipation) of nonlinear schemes are dramatically deteriorated upon activation of the nonlinear weights, and linear analysis brings little information on the actual solution behavior. For comparison purposes, we also report the ADR of the linear counterparts of the CCSSR-HW4, CCSSR-

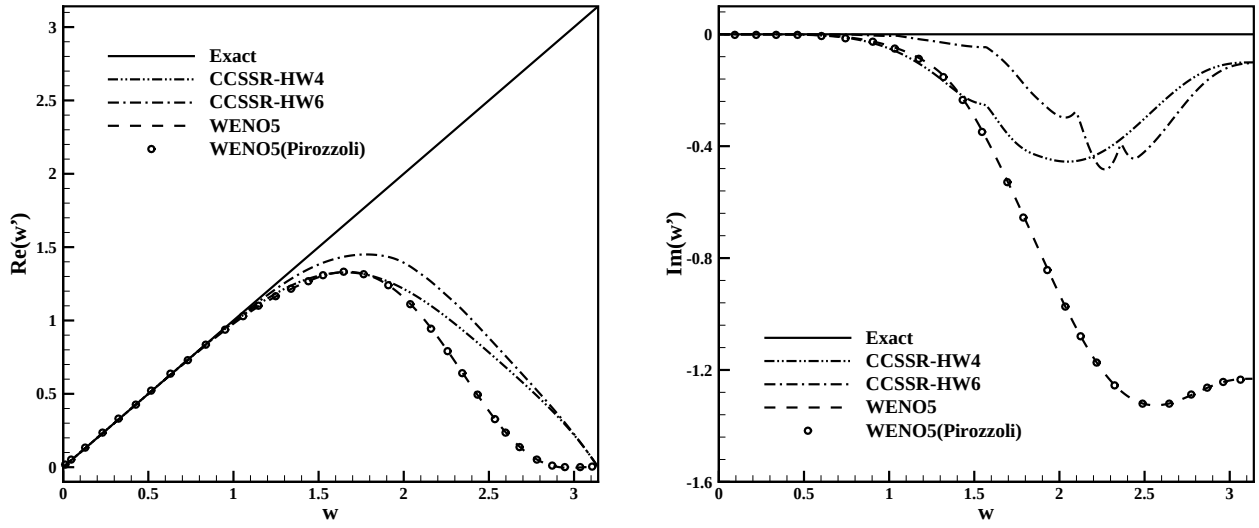

Figure 5.1: Approximate dispersion relation for the CCSSR-HW schemes and comparison with the WENO5 scheme. Left: real part of the modified wavenumber w'; Right: imaginary part of the modified wavenumber w'.

HW6 and WENO5 schemes in Figure 5.2.

In Figure 5.1, we also give the comparison for WENO5 scheme with the results of Pirozzoli [25]. We can observe that our results agree very well with the results of Pirozzoli [25]. From Figure 5.1, we can observe that the resolution of CCSSR-HW6 is better than CCSSR-HW4, and the resolution of CCSSR-HW4 is much better than the WENO5 scheme. Furthermore, the dissipation of CCSSR-HW6 is smaller than CCSSR-HW4, and the dissipation of CCSSR-HW4 is much smaller than the WENO5 scheme.

6 Numerical experiments

In this section, we apply CCSSR-HW to simulate scalar and Euler equations for some canonical problems. The optimal third order TVD Runge-Kutta method is used to evolve the solution in time.

6.1 Scalar cases

(1) Burgers' equation (e.g. [44])

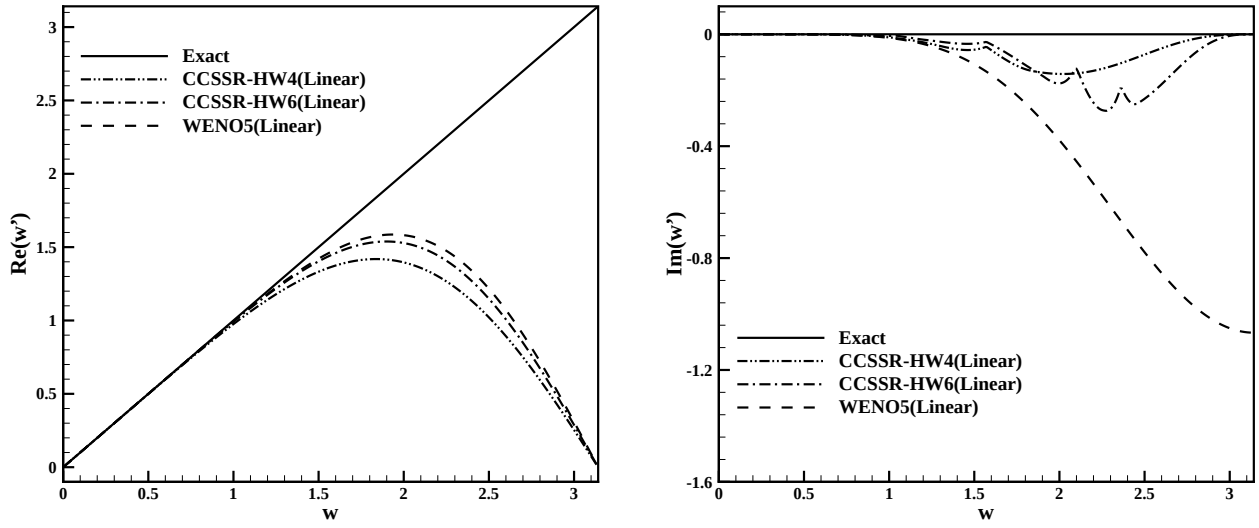

Figure 5.2: Approximate dispersion relation for the linear CCSSR-HW schemes and comparison with the linear WENO5 scheme. Left: real part of the modified wavenumber w'; Right: imaginary part of the modified wavenumber w'.

The first example is the following nonlinear scalar Burgers' equation

$$u_t + \left(\frac{u^2}{2}\right)_x = 0$$

with periodic boundary condition and the initial condition $u(x,0) = 0.5 + \sin(\pi x)$. The computational domain is taken to be [0, 2]. The solution is computed up to $t = \frac{1.5}{\pi}$ with 100 points. The CFL number is set to 0.5. The exact solution is smooth up to $t = \frac{1}{\pi}$, then it develops a moving shock which interacts with a rarefaction wave. Figure 6.1 shows the results with several different schemes. We observe that both CCSSR-HW4 and CCSSR-HW6 schemes perform as good as the WENO5 scheme. From this test, it can be concluded that the shock-capturing method proposed in this paper performs well for nonlinear problems.

(2) Buckley-Leverett problem (e.g. [14])

Our second scalar example is the Buckley-Leverett problem that is governed by the equation

$$u_t + \left(\frac{4u^2}{4u^2 + (1-u)^2}\right)_x = 0$$

with periodic boundary condition. The computational domain is taken to be [-1, 1], and the

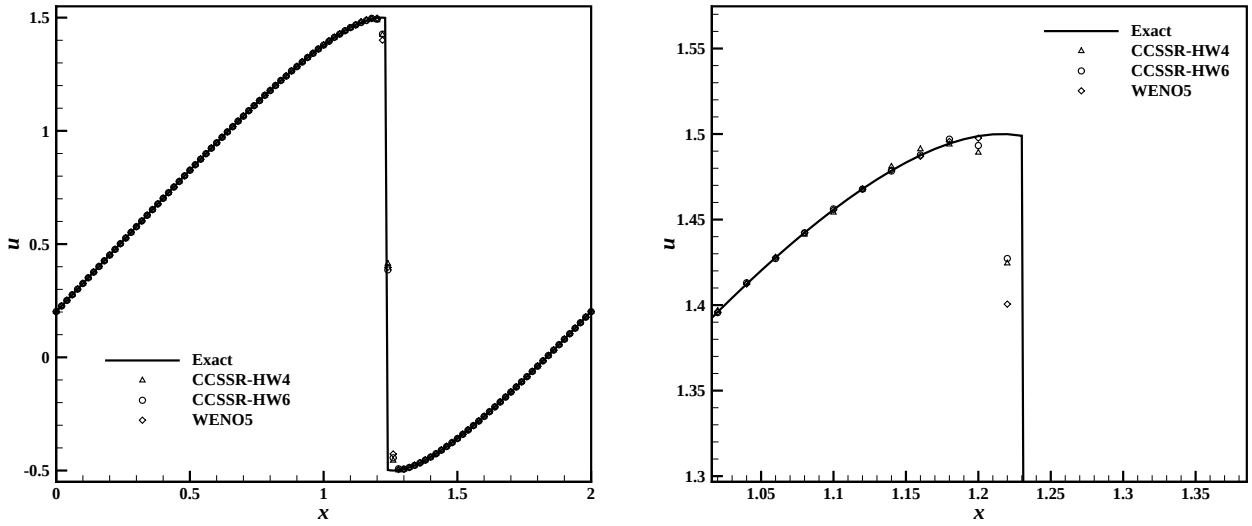

Figure 6.1: Burgers' equation, 100 points, $t = \frac{1.5}{\pi}$. Left: The results of CCSSR-HW4, CCSSR-HW6 and WENO5; Right: Locally zoomed region of the left figure.

initial condition is $u = 1$ for $-\frac{1}{2} \leq x \leq 0$ and $u = 0$ elsewhere. The solution is computed up to $t = 0.4$ with 80 points. The CFL number is set to 0.5. The exact solution is a shock-rarefaction-contact discontinuity mixture. Figure 6.2 shows the results with several different schemes. We can see that all schemes converge to the correct entropy solution and give a sharp shock profile, and the sharpness of the shock profile obtained by CCSSR-HW schemes are as good as that obtained by the WENO schemes.

6.2 One-dimensional Euler equations

(1) The Lax problem [17]

The initial condition is given by

$$(\rho, u, p) = \begin{cases} (0.445, 0.698, 3.528), & -5 \leq x < 0 \\ (0.500, 0.000, 0.571), & 0 \leq x \leq 5 \end{cases}$$

We solve the equations up to $t = 1.3$ with 100 points. The CFL number is set to 0.5. Zero time variation of the conservative variables has been specified at the left and right boundaries, which is appropriate for the time interval under interest. The numerical results for the density profiles are displayed in Figure 6.3. The CCSSR-HW schemes provide good

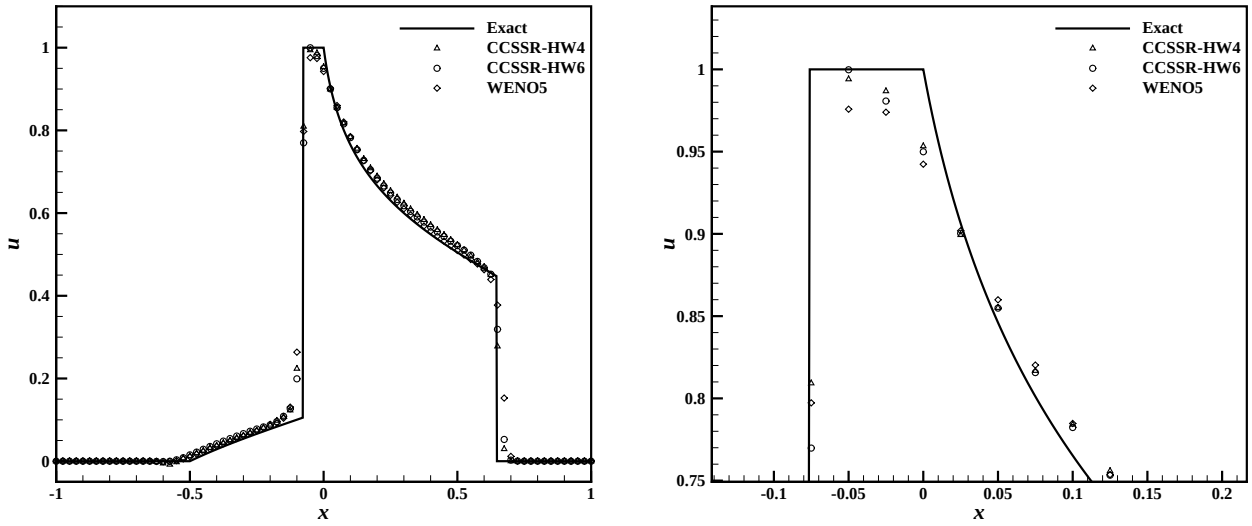

Figure 6.2: Buckley-Leverett problem, 80 points, $t = 0.4$. Left: The results of CCSSR-HW4, CCSSR-HW6 and WENO5; Right: Locally zoomed region of the left figure.

shock-capturing properties, and produce less numerical dissipation than the classical WENO schemes, especially near the discontinuities.

(2) The Sod problem [37]

The initial condition is given by

$$(\rho, u, p) = \begin{cases} (1.000, 0.000, 1.000), & -5 \le x < 0 \\ (0.125, 0.000, 0.100), & 0 \le x \le 5 \end{cases}$$

We solve the equations up to $t = 2$ with 100 points. The CFL number is set to 0.5. Zero time variation of the conservative variables has been specified at the left and right boundaries, which is appropriate for the time interval under interest. The numerical results for the density profiles are displayed in Figure 6.4. Again, we observe that the CCSSR-HW schemes provide good shock-capturing properties, and produce less numerical dissipation than the classical WENO schemes, especially near the discontinuities.

(3) Two interacting blast waves [41]

The initial condition is given by

$$(\rho, u, p) = \begin{cases} (1, 0, 1000), & 0 \le x < 0.1 \\ (1, 0, 0.01), & 0.1 \le x < 0.9 \\ (1, 0, 100), & 0.9 \le x \le 1 \end{cases}$$

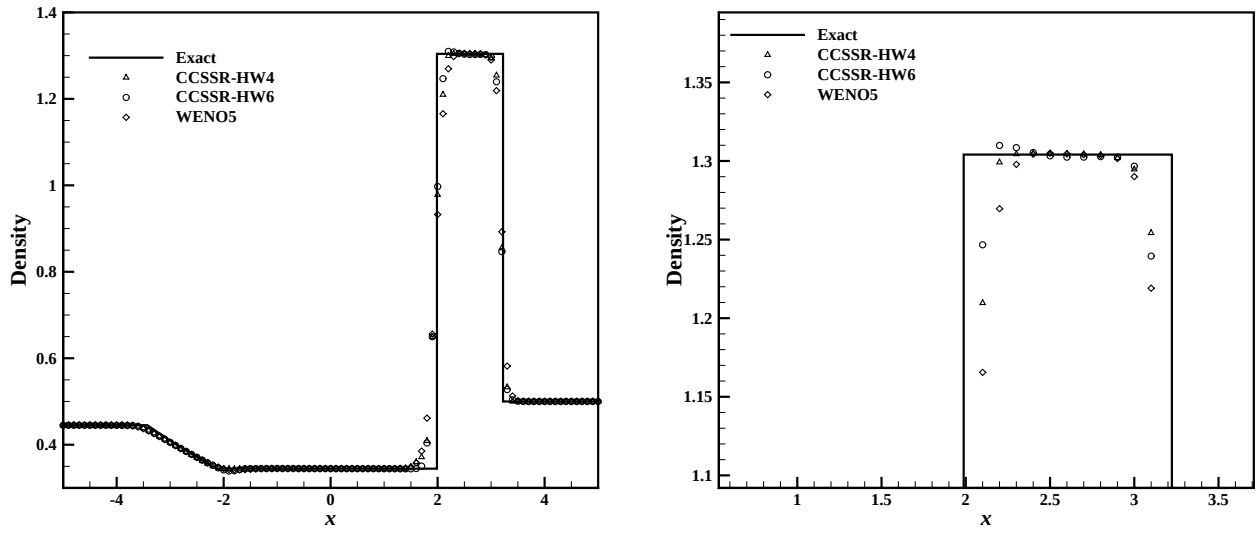

Figure 6.3: Lax problem, 100 points, $t = 1.3$. Left: The results of CCSSR-HW4, CCSSR-HW6 and WENO5; Right: Locally zoomed region of the left figure.

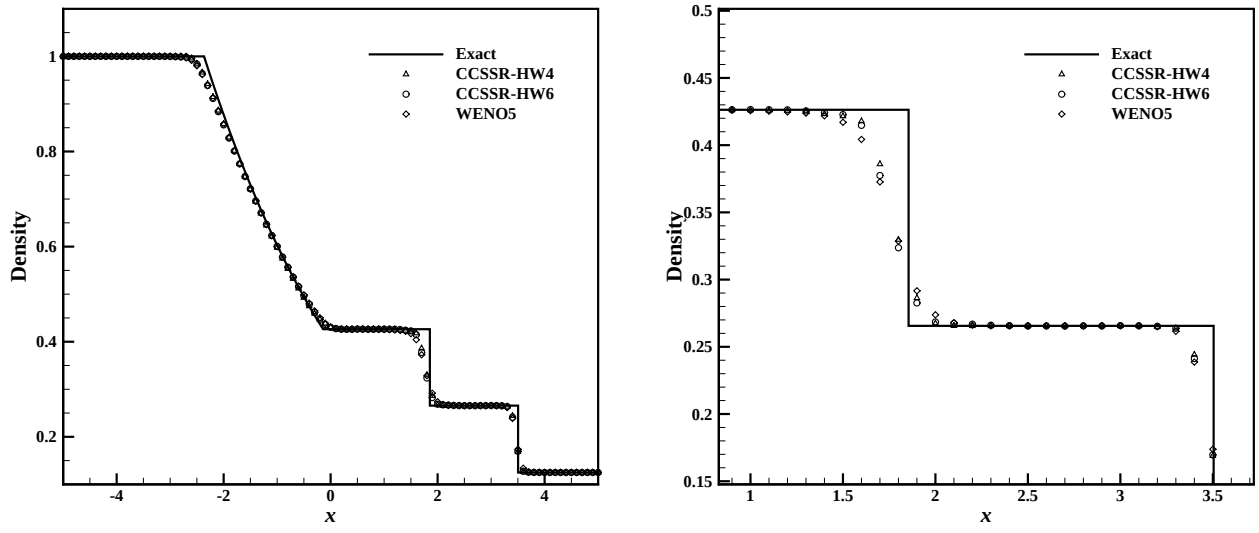

Figure 6.4: Sod problem, 100 points, $t = 2$. Left: The results of CCSSR-HW4, CCSSR-HW6 and WENO5; Right: Locally zoomed region of the left figure.

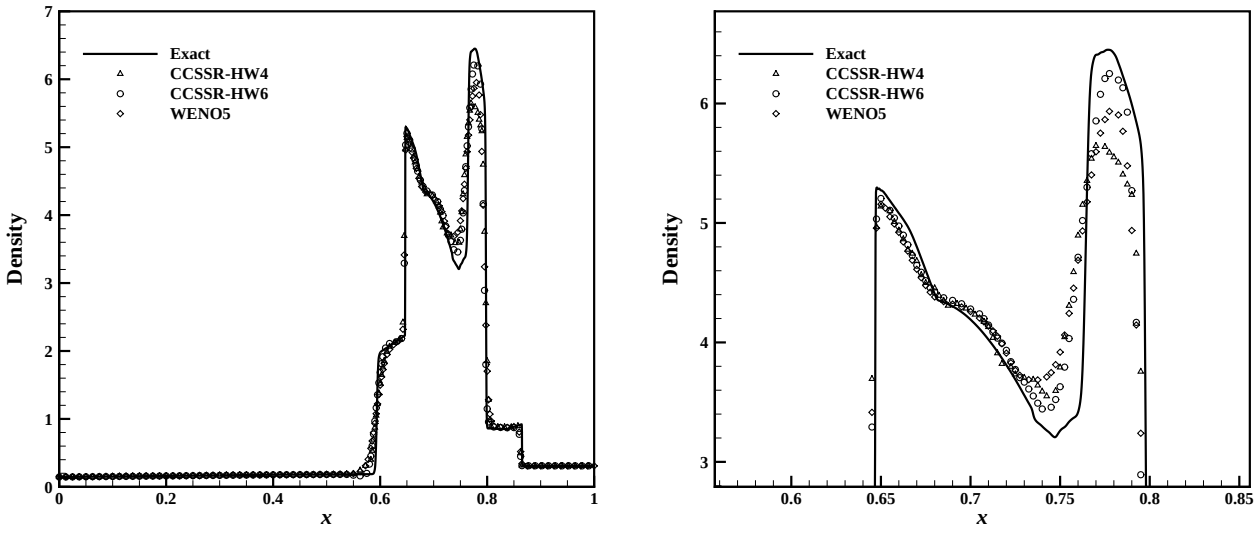

Figure 6.5: Two interacting blast waves, 400 points, $t = 0.038$. Left: The results of CCSSR-HW4, CCSSR-HW6 and WENO5; Right: Locally zoomed region of the left figure.

The reflective boundary conditions are applied at both $x = 0$ and $x = 1$. Since the exact solution is unknown, the reference solution (which can be regarded as the exact solution) is obtained by using the fifth-order WENO scheme [14] with 4000 grid points. We solve the equation up to $t = 0.038$ with 400 points. The CFL number is set to 0.5. Notice that the contact discontinuity results from the collision of the two strong shocks. Figure 6.5 compares the numerical results for density profiles with the reference solution. Again, good agreement with the reference solution is observed. Due to a smaller numerical dissipation, the CCSSR-HW schemes show an improved solution, especially near the valley and the peak, compared to the results of classical fifth-order WENO scheme. We also observe that the result of CCSSR-HW6 is better than that of WENO5, while WENO5 have a better resolution than CCSSR-HW4 at the right peak region, where the order of accuracy of scheme is more important.

(4) The Shu-Osher problem [33]

In this problem, a right-moving supersonic (Mach 3) shock wave interacts with sine waves in a density disturbance that generates a flow field with both smooth structures and

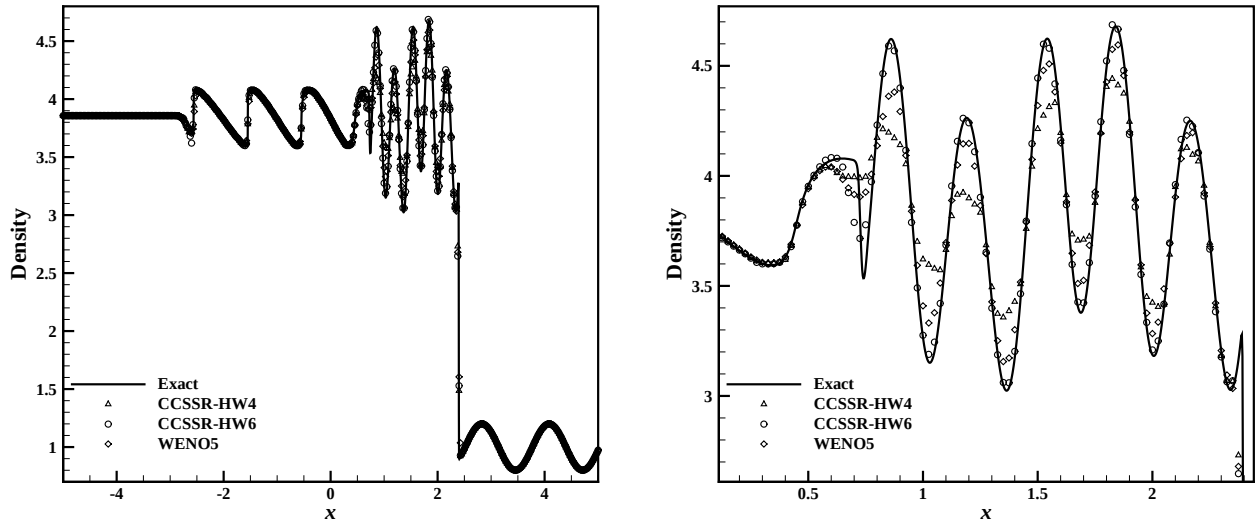

Figure 6.6: Shu-Osher problem, 400 points, $t = 1.8$. Left: The results of CCSSR-HW4, CCSSR-HW6 and WENO5; Right: Locally zoomed region of the left figure.

discontinuities. The initial condition is given by

$$(\rho, u, p) = \begin{cases} \left(\frac{27}{7}, \frac{4\sqrt{35}}{9}, \frac{31}{3}\right), & -5 \le x < -4 \\ \left(1 + \frac{1}{5}\sin(5x), 0, 1\right), & -4 \le x \le 5 \end{cases}$$

This test case is particularly severe because the solution includes smooth regions with a rich structure consisting of receding acoustic waves (that steepen and give rise to shocklets) as well as entropy waves propagating downstream of the shock. This is a model problem for shock-turbulence interaction. Since the exact solution is unknown, the reference solution (which can be regarded as the exact solution) is obtained by using the fifth-order WENO scheme [14] with 4000 grid points. We solve the equation up to $t = 1.8$ with 400 points. The CFL number is set to 0.5. Zero time variation of the conservative variables has been specified at the left and right boundaries, which is appropriate for the time interval under interest. Figure 6.6 compares the numerical results for density profiles with the exact solutions. It is clear that the CCSSR-HW6 scheme demonstrates superior resolution over the WENO5 scheme in reproducing the correct flow features downstream of the shock. However, the result of WENO5 scheme is better than that of the CCSSR-HW4 scheme.

6.3 Two-dimensional Euler equations

(1) Double Mach reflection of a strong shock [41]

The domain of the problem is [0, 4]×[0, 1] and a Mach 10 shock in air ($\gamma = 1.4$) which initially makes a $\frac{\pi}{3}$ angle with the horizontal axis. The undisturbed air ahead of the shock has density $\rho = 1.4$, pressure $p = 1.0$, and velocity $u = 0.0$, $v = 0.0$. Along the bottom boundary at $y = 0$, the short region [0, $\frac{1}{6}$] is always assigned values for the initial post-shock flow, and reflecting boundary conditions are applied to the interval [$\frac{1}{6}$,4]. This boundary condition forces the reflected shock to be "attached" to the reflecting wall. The left-hand boundary is also assigned values for the initial post-shock flow, and at the right-hand boundary, at $x = 4$, all gradients are set to zero. The values along the top boundary are set to describe the exact motion of the initial Mach 10 shock. Since there is no physical viscosity in the compressible Euler equations solved here, the developed shear layer (slip line) are purely governed by numerical viscosity. The amount of small vortices in shear layer is a good qualitative indicator of the amount of numerical viscosity, the more small vortices indicates less numerical viscosity introduced by the scheme.

We will only show the solutions on part of the domain: [0, 3] ×[0, 1], where most of the flow features are located. We use two grids: 960 × 240 points and 1920 × 480 points, which are uniform both in the x and y directions. The CFL number is set to 0.5. The final simulation time is $t = 0.2$. Figure 6.7 and Figure 6.9 show the density contours obtained by the CCSSR-HW4, CCSSR-HW6 and WENO5 schemes on the two grids. We can clearly see that the CCSSR-HW schemes have almost the same ability to capture strong shock waves as the regular WENO scheme. As shown in a close-up view of the "blow-up" region (Figure 6.8 and Figure 6.10), the CCSSR-HW schemes resolve considerably finer vortical structures. From these figures, it is evident that the CCSSR-HW schemes achieve higher resolution in the numerical results than the WENO5 scheme, especially in the region near the Mach stems where the CCSSR-HW schemes can capture the rollup of the slip line more clearly. We also observe that the result of CCSSR-HW6 is much better than that of CCSSR-HW4.

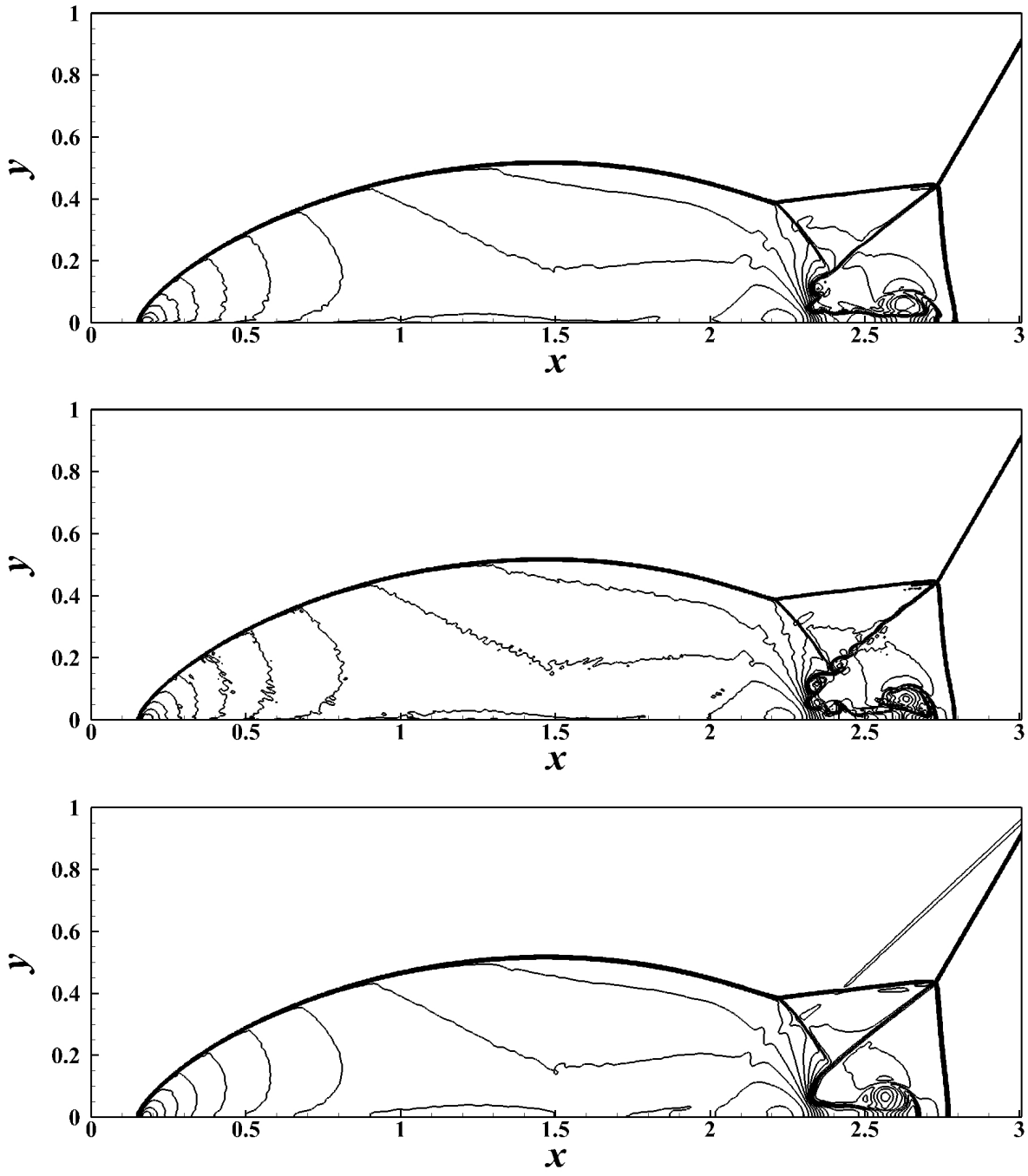

Figure 6.7: Double Mach reflection, 30 equally spaced contours for the density from 1.731 to 20.92 with uniform grid 960×240 points, $t = 0.2$. From top to bottom: CCSSR-HW4, CCSSR-HW6 and WENO5.

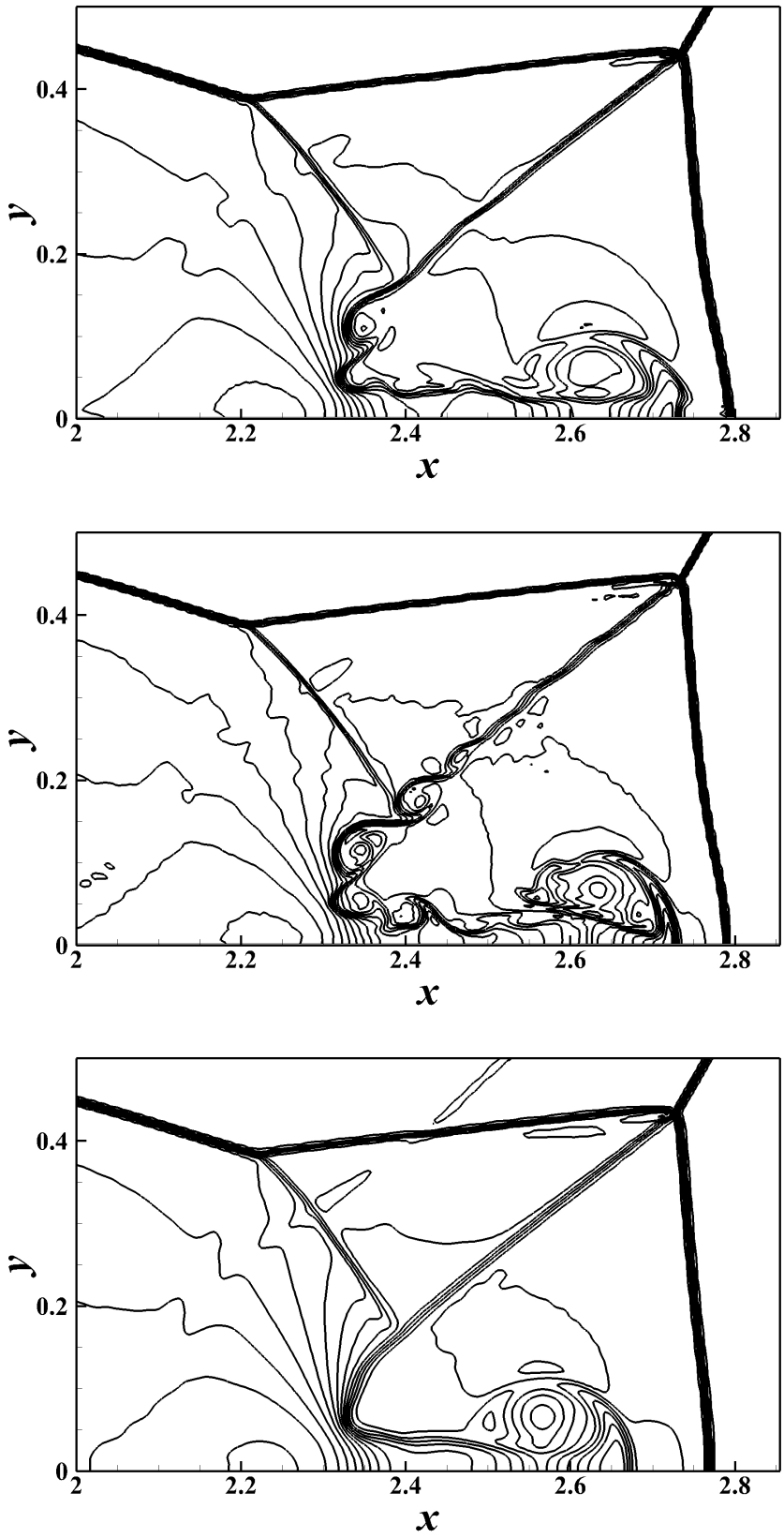

Figure 6.8: Close-up view of the "blow-up" region of Figure 6.7. From top to bottom: CCSSR-HW4, CCSSR-HW6 and WENO5.

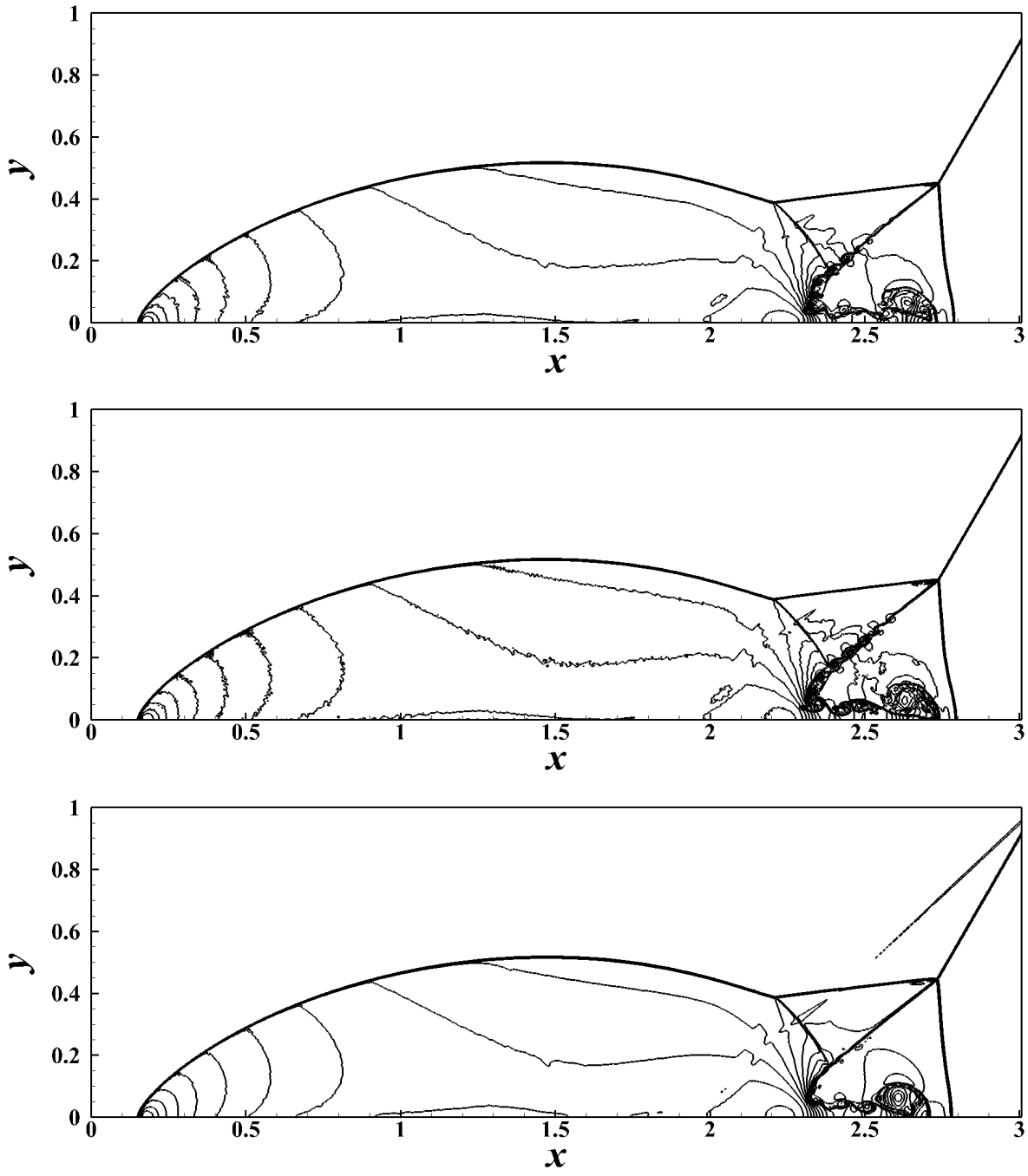

Figure 6.9: Double Mach reflection, 30 equally spaced contours for the density from 1.731 to 20.92 with uniform grid 1920×480 points, $t = 0.2$. From top to bottom: CCSSR-HW4, CCSSR-HW6 and WENO5.

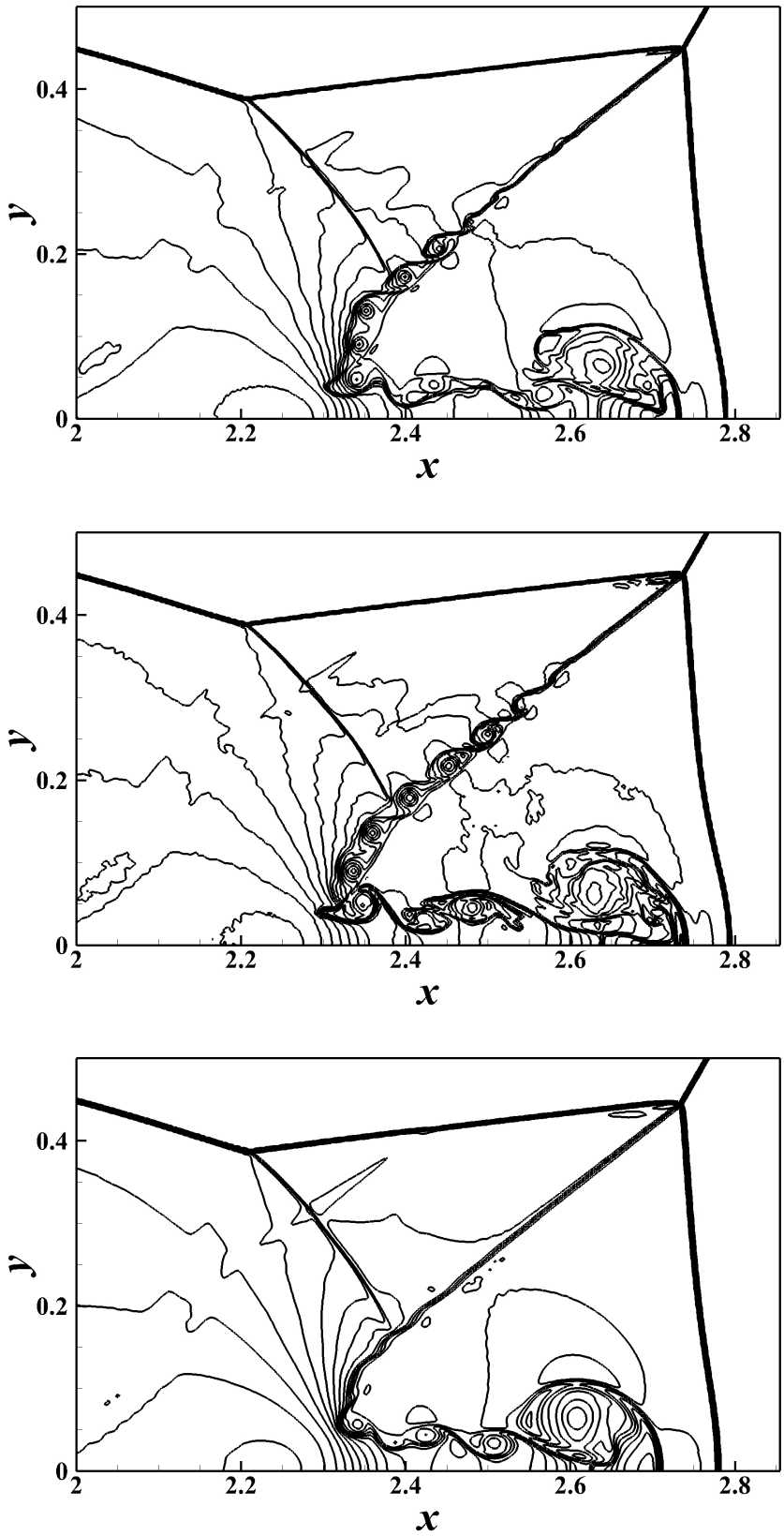

Figure 6.10: Close-up view of the "blow-up" region of Figure 6.9. From top to bottom: CCSSR-HW4, CCSSR-HW6 and WENO5.

(2) Forward facing step problem [41]

The problem is initialized by a right-going Mach 3 flow in a wind tunnel containing a step. The wind tunnel is 1 length unit wide and 3 length units long. The step is 0.2 length units high and is located 0.6 length units from the left-hand end of the tunnel. At the left is a flow-in boundary condition. Because the exit velocity is always supersonic, the exit boundary condition has no effect on the flow. Initially the wind tunnel is filled with a gamma-law gas, with $\gamma = 1.4$, which everywhere has density $\rho = 1.4$, pressure $p = 1.0$, and velocity $u = 3.0$, $v = 0.0$. Gas with this density, pressure, and velocity is continually fed in from the left-hand boundary. Reflective boundary conditions are applied along the walls of the tunnel. The corner of the step is the center of a rarefaction fan and hence is a singular point of the flow. For the treatment of the singularity at the corner of the step, we adopt the same technique used in [41], which is based on the assumption of a nearly steady flow in the region near the corner.

We use two grids: 480×160 points and 960×320 points, which are uniform both in the x and y direction. The CFL number is set to 0.5. The final simulation time is $t = 4$. In Figures 6.11-6.12, we show the density component in the wind tunnel obtained by all three schemes on the two grids. From these figures, we can conclude that the CCSSR-HW schemes achieve higher resolution in the numerical results than the WENO5 scheme, especially in the shear layer region where the CCSSR-HW schemes can capture the rollup of the vortices more clearly. We also observe that the result of CCSSR-HW6 is much better than that of CCSSR-HW4.

(3) Rayleigh-Taylor instability (e.g. [31])

This problem is used as a test case with the following initial data:

$$(\rho, u, v, p) = \begin{cases} (2, 0, -0.025a \cdot \cos(8\pi x), 2y + 1), & 0 \le y < \frac{1}{2} \\ (1, 0, -0.025a \cdot \cos(8\pi x), y + \frac{3}{2}), & \frac{1}{2} \le y \le 1 \end{cases}$$

where a is the sound speed, $a = \sqrt{\frac{\gamma p}{\rho}}$. The computational domain is taken to be $[0, \frac{1}{4}] \times [0, 1]$. The ratio of specific heat $\gamma = \frac{5}{3}$. A source term $S = (0, 0, \rho, \rho v)$ is added to the

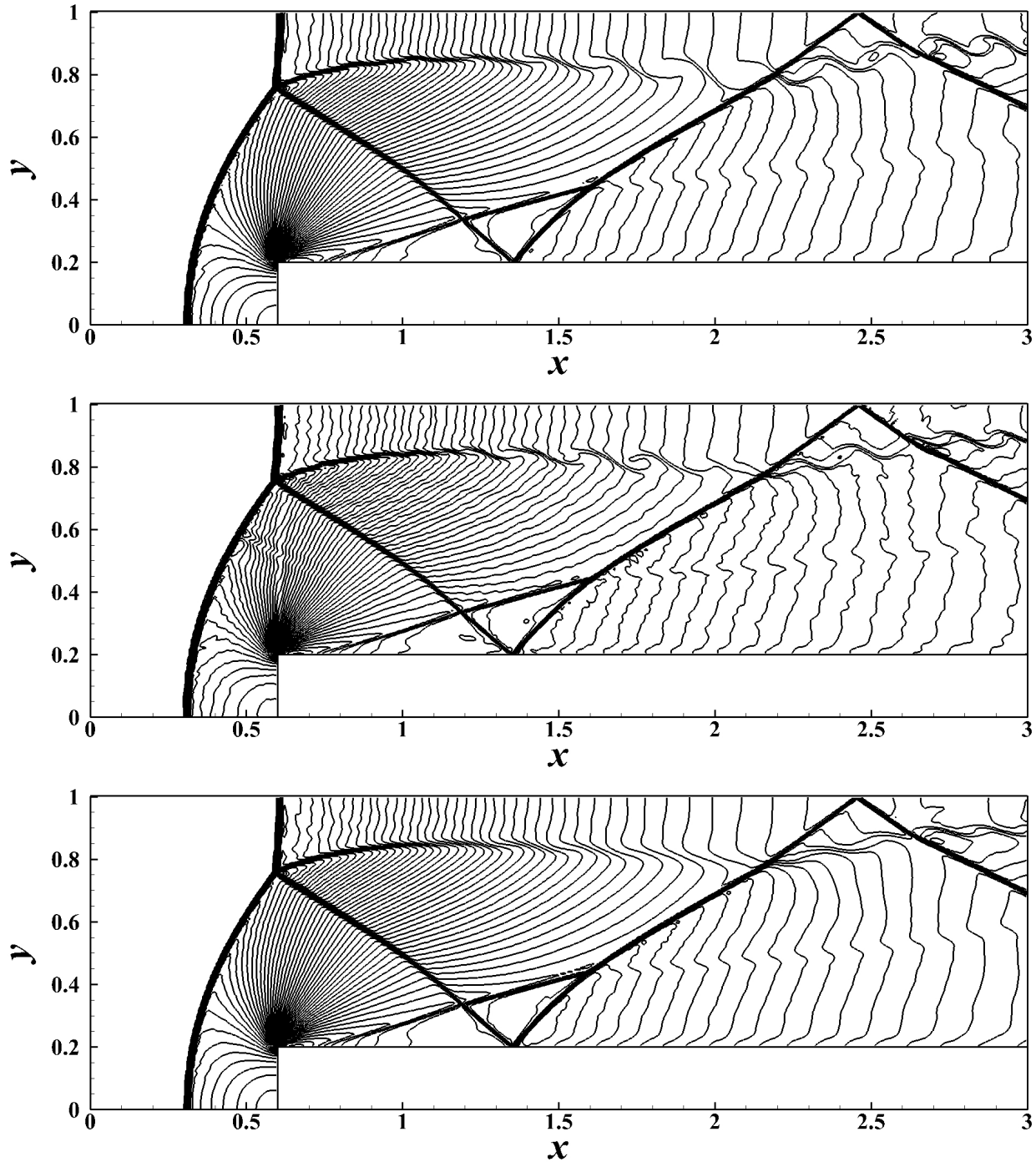

Figure 6.11: Forward facing step problem, 60 equally spaced contours for the density from 0.2568 to 6.607 with uniform grid 480×160 points, $t = 4$. From top to bottom: CCSSR-HW4, CCSSR-HW6 and WENO5.

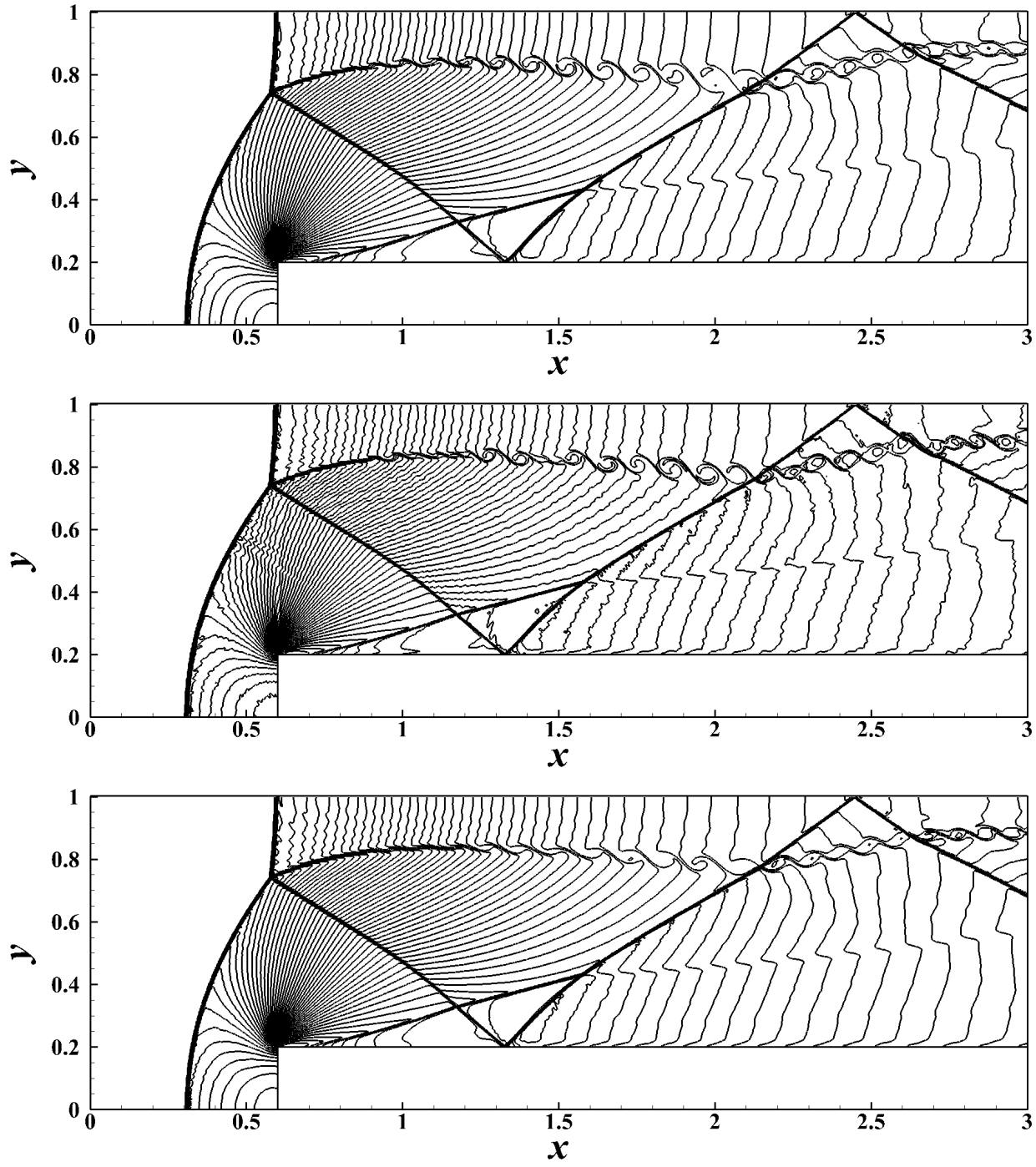

Figure 6.12: Forward facing step problem, 60 equally spaced contours for the density from 0.2568 to 6.607 with uniform grid 960×320 points, $t = 4$. From top to bottom: CCSSR-HW4, CCSSR-HW6 and WENO5.

two dimensional Euler equations. Reflective boundary conditions are implemented at the left and right boundaries. At the top boundary, the flow values are set as $(\rho, u, v, p) = (1, 0, 0, 2.5)$. At the bottom boundary, the flow values are set as $(\rho, u, v, p) = (2, 0, 0, 1)$. The realistic solution of this problem should contain a rich flow structure caused by the instability. This may be achieved by solving the Navier-Stokes equations numerically with small numerical viscosity. Therefore, this problem is very important for determining the magnitude of numerical dissipation of various high-order shock-capturing schemes. The appearance of a fine structure by solving the Euler equations with such shock-capturing scheme gives an idea of how well the scheme is performing.

We use two grids: 60×240 points and 120×480 points, which are uniform both in the x and y direction. The CFL number is set to 0.5. The final simulation time is $t = 1.95$. In Figures 6.13-6.14, we show the density component obtained by all three schemes on the two grids. From these figures, we can conclude that the CCSSR-HW schemes achieve higher resolution numerical results as compared to the WENO5 scheme, especially in the shear layer region where the CCSSR-HW schemes can capture the rollup of the vortices and the small features with increased grid resolution more clearly. We also observe that the result of CCSSR-HW6 is much better than that of CCSSR-HW4.

7 Concluding remarks

In this paper, we develop our previous linear central compact schemes [20] to nonlinear compact schemes by introducing a hybrid weighted interpolation of an upwind interpolation and a central interpolation. Through systematical analysis of the dispersion and dissipation characteristics by approximating dispersion relation (ADR) technique of Pirozzoli [25], we show that the present nonlinear compact schemes have higher resolution and lower dissipation than regular WENO schemes, while their ability to compute strong shock wave is almost the same with that of regular WENO schemes.

Numerical tests to a series of typical problems including nonlinear scalar equations, shock

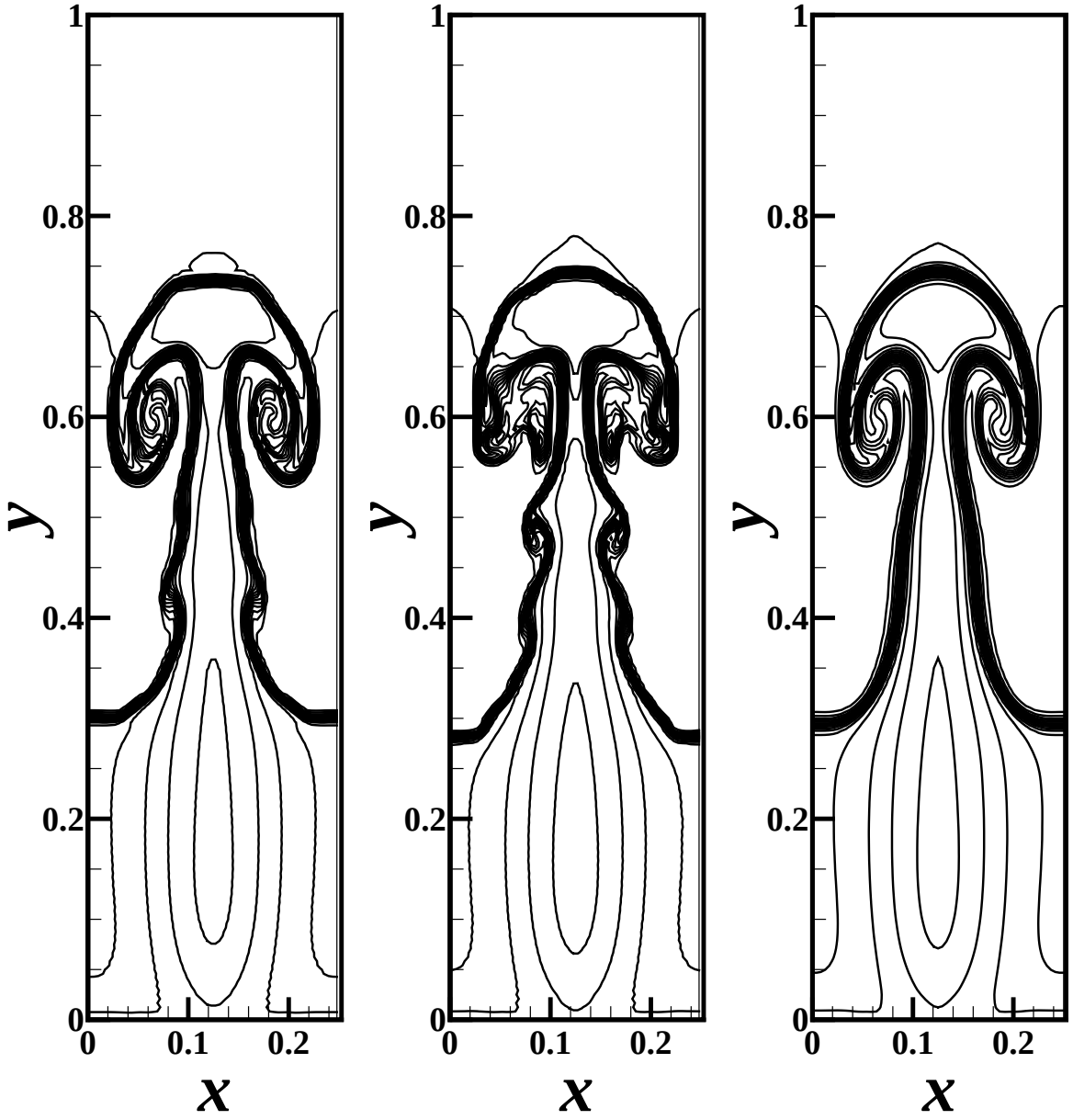

Figure 6.13: Rayleigh-Taylor instability, 15 equally spaced contours for the density from 0.952269 to 2.14589 with uniform grid 60×240 points, $t = 1.95$. From left to right: CCSSR-HW4, CCSSR-HW6 and WENO5.

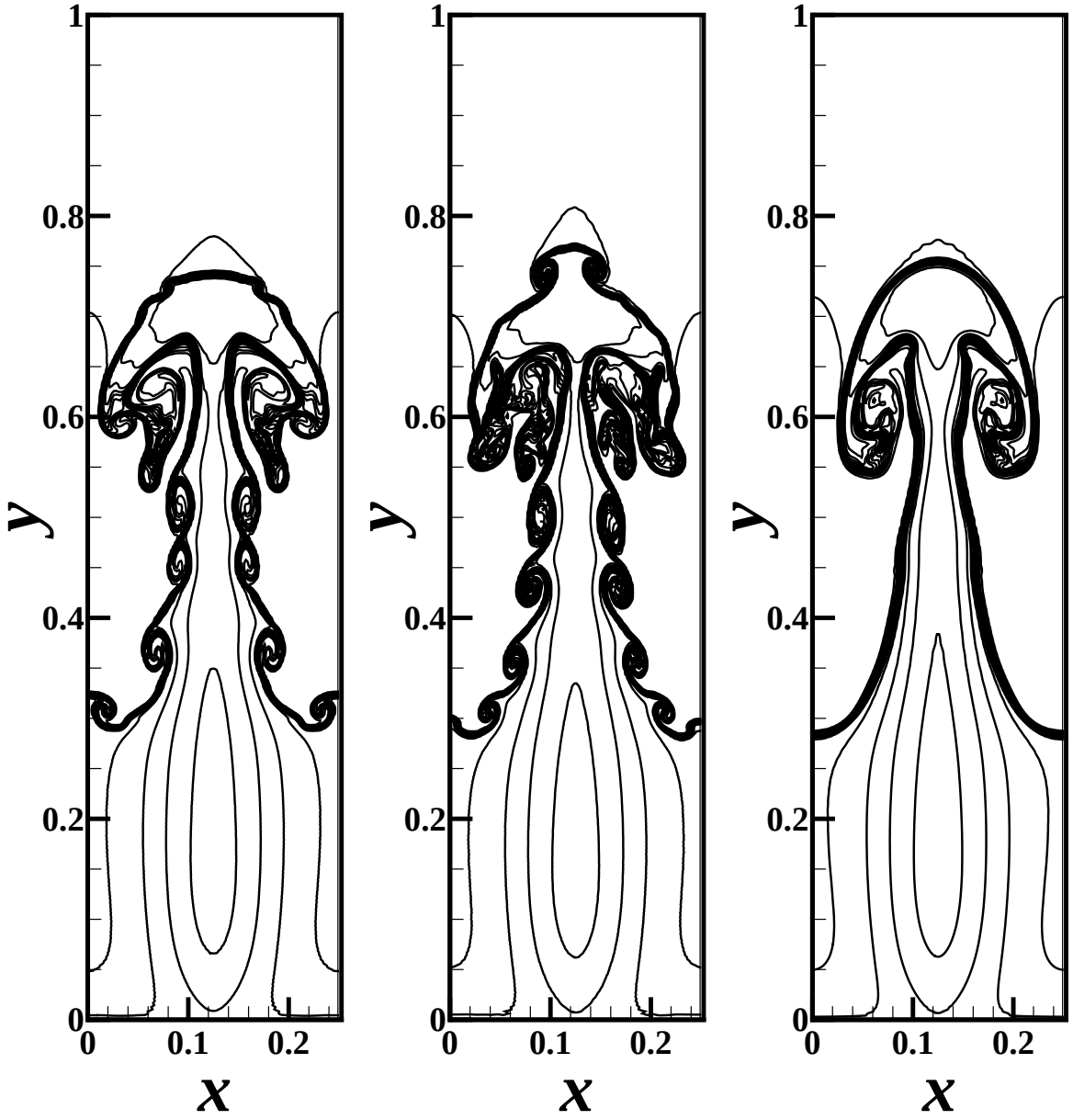

Figure 6.14: Rayleigh-Taylor instability, 15 equally spaced contours for the density from 0.952269 to 2.14589 with uniform grid 120×480 points, $t = 1.95$. From left to right: CCSSR-HW4, CCSSR-HW6 and WENO5.

tube problems, double Mach reflection, forward facing step problem and Rayleigh-Taylor instability are implemented by solving one-dimensional and two-dimensional Euler equations. A systematic comparison with regular WENO schemes is made. The results of the numerical experiments show that the present scheme is a suitable candidate for direct numerical simulation of multiscale problems such as turbulent flows and aeroacoustics.

References

[1] N.A. Adams, K. Shariff, A high-resolution hybrid compact-ENO scheme for shock-turbulence interaction problems, Journal of Computational Physics 127 (1996) 27-51.

[2] M. Arora, P.L. Roe, On postshock oscillations due to shock capturing schemes in unsteady flows, Journal of Computational Physics 130 (1997) 25-40.

[3] D. Balsara, C.-W. Shu, Monotonicity preserving weighted essentially non-oscillatory schemes with increasingly high order of accuracy, Journal of Computational Physics 160 (2000) 405-452.

[4] R. Borges, M. Carmona, B. Costa, W.S. Don, An improved weighted essentially non-oscillatory scheme for hyperbolic conservation laws, Journal of Computational Physics 227 (2008) 3191-3211.

[5] B.J. Boersma, A staggered compact finite difference formulation for the compressible Navier-Stokes equations, Journal of Computational Physics 208 (2005) 675-690.

[6] E. Carlini, R. Ferretti, G. Russo, A weighted essentially nonoscillatory, large timestep scheme for Hamilton-Jacobi equations, SIAM Journal on Scientific Computing 27 (2005) 1071-1091.

[7] B. Cockburn, C.-W. Shu, Nonlinearly stable compact schemes for shock calculations, SIAM Journal on Numerical Analysis 31 (1994) 607-627.

[8] X. Deng, H. Zhang, Developing high-order weighted compact nonlinear schemes, Journal of Computational Physics 165 (2000) 22-44.

[9] S.K. Godunov, A finite-difference method for the numerical computation of discontinuous solutions of the equations of fluid dynamics, Mat. Sb. 47 (1959) 271-306.

[10] S. Gottlieb, C.-W. Shu, Total variation diminishing Runge-Kutta schemes, Mathematics of Computation 67 (1998) 73-85.

[11] A. Harten, B. Engquist, S. Osher, S.R. Chakravarthy, Uniformly high order accurate essentially non-oscillatory schemes, III, Journal of Computational Physics 71 (1987) 231-303.

[12] A.K. Henrick, T.D. Aslam, J.M. Powers, Mapped weighted essentially non-oscillatory schemes: Achieving optimal order near critical points, Journal of Computational Physics 207 (2005) 542-567.

[13] X.Y. Hu, Q. Wang, N.A. Adams, An adaptive central-upwind weighted essentially non-oscillatory scheme, Journal of Computational Physics 229 (2010) 8952-8965.

[14] G.-S. Jiang, C.-W. Shu, Efficient implementation of weighted ENO schemes, Journal of Computational Physics 126 (1996) 202-228.

[15] L. Jiang, H. Shan, C.Q. Liu, Weighted Compact Scheme for Shock Capturing, International Journal of Computational Fluid Dynamics, 15 (2001) 147-155.

[16] E. Johnsen, J. Larsson, A.V. Bhagatwala, W.H. Cabot, P. Moin, et al., Assessment of high-resolution methods for numerical simulations of compressible turbulence with shock waves, Journal of Computational Physics 229 (2010) 1213-1237.

[17] P.D. Lax, Weak solutions of nonlinear hyperbolic equations and their numerical computation, Communications on Pure and Applied Mathematics 7 (1954) 159-193.

[18] S.K. Lele, Compact finite difference schemes with spectral-like resolution, Journal of Computational Physics 103 (1992) 16-42.

[19] X.-D. Liu, S. Osher, T. Chan, Weighted essentially non-oscillatory schemes, Journal of Computational Physics 115 (1994) 200-212.

[20] X. Liu, S. Zhang, H. Zhang, C-W. Shu, A new class of central compact schemes with spectral-like resolution I: Linear schemes, Journal of Computational Physics 248 (2013) 235-256.

[21] K. Mahesh, A family of high order finite difference schemes with good spectral resolution, Journal of Computational Physics 145 (1998) 332-358.

[22] M.P. Martin, E.M. Taylor, M. Wu, V.G. Weirs, A bandwidth-optimized WENO scheme for the effective direct numerical simulation of compressible turbulence, Journal of Computational Physics 220 (2006) 270-289.

[23] S. Nagarajan, S.K. Lele, J.H. Ferziger, A robust high-order compact method for large eddy simulation, Journal of Computational Physics 191 (2003) 392-419.

[24] S. Pirozzoli, Conservative hybrid compact-WENO schemes for shock-turbulence interaction, Journal of Computational Physics 178 (2002) 81-117.

[25] S. Pirozzoli, On the spectral properties of shock-capturing schemes, Journal of Computational Physics 219 (2006) 489-497.

[26] S. Pirozzoli, Numerical methods for high-speed flows, Annual Review of Fluid Mechanics 43 (2011) 163-194.

[27] D. Ponziani, S. Pirozzoli, F. Grasso, Development of optimized weighted-ENO schemes for multiscale compressible flows, International Journal for Numerical Methods in Fluids 42 (2003) 953-977.

[28] Y. Ren, M. Liu, H. Zhang, A characteristic-wise hybrid compact-WENO scheme for solving hyperbolic conservation laws, Journal of Computational Physics 192 (2003) 365-386.

[29] P.L. Roe, Approximate Riemann solvers, parameter vectors and difference schemes, Journal of Computational Physics 43 (1981) 357-372.

[30] K. Sebastian, C.-W. Shu, Multidomain WENO finite difference method with interpolation at subdomain interfaces, Journal of Scientific Computing 19 (2003) 405-438.

[31] J. Shi, Y.-T. Zhang, C.-W. Shu, Resolution of high order WENO schemes for complicated flow structures, Journal of Computational Physics 186 (2) (2003) 690-696.

[32] C.-W. Shu, S. Osher, Efficient implementation of essentially non-oscillatory shock capturing schemes, Journal of Computational Physics 77 (1988) 439-471.

[33] C.-W. Shu, S. Osher, Efficient implementation of essentially non-oscillatory shock-capturing schemes II, Journal of Computational Physics 83 (1989) 32-78.

[34] C.-W. Shu, Essentially non-oscillatory and weighted essentially non-oscillatory schemes for hyperbolic conservation laws, in: B. Cockburn, C. Johnson, C.-W. Shu, E. Tadmor (Eds.), Advanced Numerical Approximation of Nonlinear Hyperbolic Equations, in: A. Quarteroni (Ed.), Lecture Notes in Mathematics, vol. 1697, Springer, Berlin, 1998, pp. 325-432.

[35] C.-W. Shu, High order weighted essentially nonoscillatory schemes for convection dominated schemes, SIAM Review 51 (2009) 82-126.

[36] R.K. Shukla, X. Zhong, Derivation of high-order compact finite difference schemes for non-uniform grid using polynomial interpolation, Journal of Computational Physics 204 (2005) 404-429.

[37] G. Sod, A survey of several finite difference methods for systems of nonlinear hyperbolic conservation laws, Journal of Computational Physics 27 (1978) 1-31.

[38] C.K.W. Tam, J.C. Webb, Dispersion-relation-preserving finite difference schemes for computational acoustics, Journal of Computational Physics 107 (1993) 262-281.

[39] M.R. Visbal, D.V. Gaitonde, On the use of higher-order finite-difference schemes on curvilinear and deforming meshes, Journal of Computational Physics 181 (2002) 155-185.

[40] Z.J. Wang, R.F. Chen, Optimized weighted essentially nonoscillatory schemes for linear waves with discontinuity, Journal of Computational Physics 174 (2001) 381- 404.

[41] P. Woodward, P. Colella, The numerical simulation of two-dimensional fluid flow with strong shocks, Journal of Computational Physics 54 (1984) 115-173.

[42] N.K. Yamaleev, M.H. Carpenter, Third-order energy stable WENO scheme, Journal of Computational Physics 228 (8) (2009) 3025-3047.

[43] N.K. Yamaleev, M.H. Carpenter, A systematic methodology for constructing high-order energy stable WENO schemes, Journal of Computational Physics 228 (2009) 4248-4272.

[44] S. Zhang, S. Jiang, C.-W. Shu, Development of nonlinear weighted compact schemes with increasingly higher order accuracy, Journal of Computational Physics 227 (2008) 7294-7321.